

A Stochastic Framework for Continuous-Time State Estimation of Continuum Robots

Spencer Teetaert, *Graduate Student Member, IEEE*, Sven Lilge, *Member, IEEE*, Jessica Burgner-Kahrs, *Senior Member, IEEE*, Timothy D. Barfoot, *Fellow, IEEE*

Abstract—State estimation techniques for continuum robots (CRs) typically involve using computationally complex dynamic models, simplistic shape approximations, or are limited to quasi-static methods. These limitations can be sensitive to unmodelled disturbances acting on the robot. Inspired by a factor-graph optimization paradigm, this work introduces a continuous-time stochastic state estimation framework for continuum robots. We introduce factors based on continuous-time kinematics that are corrupted by a white noise Gaussian process (GP). By using a simple robot model paired with high-rate sensing, we show adaptability to unmodelled external forces and data dropout. The result contains an estimate of the mean and covariance for the robot’s pose, velocity, and strain, each of which can be interpolated continuously in time or space. This same interpolation scheme can be used during estimation, allowing for inclusion of measurements on states that are not explicitly estimated. Our method’s inherent sparsity leads to a linear solve complexity with respect to time and interpolation queries in constant time. We demonstrate our method on a CR with gyroscope and pose sensors, highlighting its versatility in real-world systems.

Index Terms—Probability and Statistical Methods, Flexible Robots, Dynamics, State Estimation

I. INTRODUCTION

Continuum robots (CRs) are jointless, flexible, and easily miniaturizable manipulators capable of bending into contorted spatial shapes. They are often said to be inspired by the animal kingdom, resembling the motion of snakes, elephant trunks, or worms [1]. Their unique properties allow them to navigate in confined and cluttered environments. This makes them particularly suitable for applications such as minimally invasive surgery [2], [3], industrial inspection and repair in hard-to-reach places [4], [5], as well as search and rescue operations in disaster areas [6].

To date, great progress has been made on the modeling of continuum robots [7], using a variety of kinematic, static, and dynamic assumptions and approaches. Such methods aim to accurately predict the robot’s shape given its material properties, actuation, and external loads, which is crucial for the aforementioned applications. However, they are usually prone to inaccuracies arising from both unmodelled effects and unknown contact forces during interaction with the environment. This makes the application of open-loop model-based control approaches [8] challenging and motivates the integration of additional sensing to account for such model inaccuracies. Here, state estimation approaches that can fuse

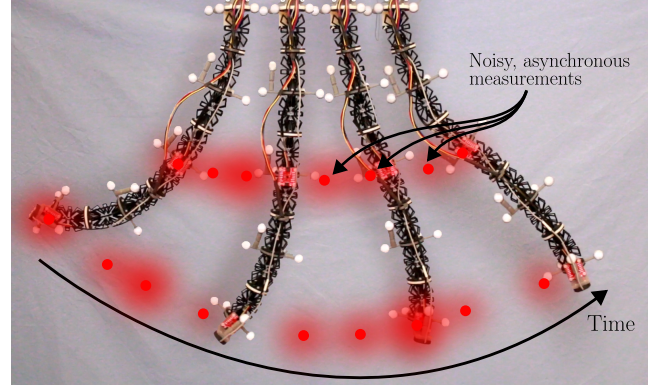


Fig. 1. A CR moving through time, taking asynchronous and noisy measurements of its state. This situation arises in practical scenarios where multiple high-rate sensors are used on the robot. In such scenarios, data from multiple high-rate sensors produce update rates much faster than a CR shape can reasonably be solved for. In this work, we propose addressing this issue by using a physically motivated Gaussian process prior defined over both space and time that is capable of continuous-time interpolation in constant time. This efficient interpolation can be used to fuse high-rate measurements from multiple sensors at slower time steps while maintaining accurate estimates in between time steps.

sensor feedback on the robot’s state with appropriate model prediction become particularly important. This is especially true as real world data is noisy. Fig. 1 illustrates such a scenario where a continuum robot (CR) is moving through time, taking asynchronous and noisy measurements of its state.

A. Related Work

In the following, we review the most relevant related work on the state estimation of continuum robots. During the review, we differentiate between non-probabilistic and probabilistic methods. Both approaches consider quantities such as actuation and measurements to compute a resulting continuum robot state. The definition of the robot state varies by work, but commonly includes the robot’s pose, strain, and/or velocity, and occasionally contains higher derivatives such as acceleration or the strain gradient. However, probabilistic approaches explicitly take into account the uncertainties of both the underlying prior model and the noisy measurements, weighing them appropriately. This additionally allows for computing a distribution of possible robot states, where the mean is the most likely state and the covariance is its uncertainty.

1) *Non-probabilistic Methods*: Non-probabilistic estimation methods usually employ optimization approaches to fit kinematic, static, or dynamic models to discretely sensed quantities, such as pose or strain.

This work was supported in part by the National Sciences and Engineering Research Council of Canada (NSERC) and the Ontario Graduate Scholarship.

The authors are with the University of Toronto Robotics Institute, Toronto, ON, Canada. (e-mail: spencer.teetaert@robotics.utoronto.ca).

Examples of fitting kinematic shape representations include optimizing constant-curvature arcs [9], Bézier curves [10], or polynomial-curvature models [11], [12] to minimize the deviation between the robot’s centerline and the corresponding measurements. More recently, a model-based shape reconstruction framework based on a finite-element analysis (FEA) simulation was proposed, incorporating readings of distributed strain sensors into an optimization routine [13]. In [14], a piecewise-constant-curvature representation is fit to orientation readings from an inertial measurement unit (IMU), while accounting for measurement drift. By relying not only on current measurements but also incorporating the history of readings, a sliding-window estimator is presented in [15], which fuses a series of past IMU measurements at the robot’s tip with a constant-curvature model.

Instead of solely relying on kinematic representations, some approaches incorporate assumptions and knowledge about the mechanics of continuum robots by fitting appropriate static models to measurement data. Examples include using static models based on the principle of virtual power [16] and pseudo-rigid-body assumptions [17]. Similarly, more recent approaches are additionally considering the dynamic mechanical properties of continuum robots, by fusing dynamic Cosserat-rod models, expressing the robot’s state as a function of space and time, with sensed quantities. For instance, the works in [18]–[20] fuse velocity and load measurements at the boundaries of the robot’s shape (i.e., at its tip and base) with the partial differential equations of a dynamic Cosserat-rod model. In [21], a dynamic state estimation approach of soft robots is proposed, which only relies on sensing of the actuation values and known external forces.

Lastly, approaches that leverage learned models to estimate the shape of continuum robots have started to attract increasing attention. In one example, a neural network is employed to predict control points used for a continuous shape interpolation based on strain-gauge readings [22]. In another example, fiber Bragg grating (FBG), orientation, and position measurements are used to estimate continuum robot shapes utilizing a physics-informed neural network [23].

2) *Probabilistic Methods*: Most probabilistic state estimation approaches aim to track the evolution of a chosen continuum robot state representation over time, typically using filtering techniques. For instance, the works [24] and [25] both rely on a constant-curvature representation, tracking its arc parameters over time using particle filters to estimate a catheter’s tip pose or position, respectively. Similar approaches include [26]–[31], all of which implement discrete-time extended or unscented Kalman filters to estimate the piecewise-constant-curvature parameters of multi-backbone, tendon-driven, or pneumatic continuum robots over time.

Instead of relying on constant-curvature representations, some approaches utilize modal basis functions, enabling higher-order and potentially more accurate descriptions of the continuum robot’s shape and deformations. In [32], learned shape basis functions are chosen to represent the continuum robot’s shape, tracking their coefficients with a probabilistic filter implementation for estimation over time. The use of several polynomial shape basis function representations of

different orders is proposed in [33], which implements a discrete-time extended Kalman filter for the shape estimation of tendon-driven continuum robots.

Finally, there exists a class of probabilistic state estimation approaches that rely on variable-curvature representations to estimate the shape of continuum robots. A key distinction from the previously discussed methods is that these approaches are currently employed almost exclusively in a quasi-static manner. Rather than estimating the robot’s state over time, they compute a continuous estimate of its state along the robot’s length at a single point in time. This is achieved by applying probabilistic filtering or smoothing over the robot’s arclength, rather than over time as in earlier examples.

One example of such an approach is presented in [34], where a Rauch–Tung–Striebel (RTS) smoother is applied over arclength to estimate the smooth, continuous state of a concentric tube robot. The method relies on numerical integration to solve the ordinary differential equations derived from a Cosserat-rod statics model. This approach was later extended to coupled parallel continuum robots in [35]. Alternatively, recent work proposes the usage of Gaussian process regression over arclength to estimate the smooth continuum robot state [36], re-purposing methods from the continuous-time estimation literature [37]. Here, a simplified static Cosserat-rod-based prior is proposed, allowing stochastic integration in closed form, enabling fast computation times during estimation. Recent work on this approach includes an extension to handle coupled parallel continuum robots [38], the incorporation of known actuation inputs [39], as well as the estimation of external loads in addition to estimating the robot’s shape [40].

Looking at the current state of probabilistic state estimation approaches for continuum robots, it can be seen that most methods rely on simplifying kinematic representations, such as constant-curvature assumptions or polynomial shape basis functions [26], [28], [30], [32], [33]. These approaches typically employ filters that operate in a discrete-time manner, requiring a state estimation update whenever a measurement becomes available and restricting the estimated robot state to these discrete update times. Variable-curvature frameworks, on the other hand, are currently limited to quasi-static scenarios [36], [40], [41]. While dynamic variable-curvature estimation methods do exist, they rely heavily on detailed modeling assumptions and prior system knowledge [18]–[21]. Additionally, they are restricted to non-probabilistic formulations, limiting their ability to incorporate model and measurement uncertainties. As such, a lack of probabilistic methods capable of estimating the smooth state of continuum robots continuously over both time and arclength, while explicitly accounting for noise and uncertainty, can be identified.

B. Contributions

In this work, we address this gap by proposing a physically motivated Gaussian-process prior defined over both space and time, unifying continuous-time [37] with continuous-arclength [36] estimation into a single framework. This enables continuous estimation of the robot’s state over time at every

arclength included in the solve, and over arclength at each timestep included in the solve. Preliminary work aiming to address this gap was proposed in [42]. However, the work remains mostly incomplete and unvalidated.

To the best of our knowledge, this work represents the first stochastic state estimator for continuum robots that is continuous in time. The proposed method supports efficient handling of high-rate and asynchronous measurements with minimal computational overhead. We validate our approach through both simulation and experimental evaluation, using pose, strain, and velocity measurements on a tendon-driven continuum robot. Our experimental results highlight the method's ability to capture dynamic effects in the robot's motion, handle data dropout, and benefit from sensor fusion. An open-source implementation of this project is made publicly available to the research community at <https://github.com>.

II. METHODOLOGY

A. Notation

Throughout this work, we use the notation from Chapter 8 of [43], specific details of which can be found in Appendix A. A result of this notation that we highlight here includes representing robot pose transformation matrices as an inertial frame (denoted i) expressed in the robot body frame (denoted b). Given this notation, the kinematic equation for a pose with some generalized body-centric velocity $\varpi_b(t) \in \mathbb{R}^6$ is given by

$$\frac{\partial T_{bi}(t)}{\partial t} = \varpi_b(t)^\wedge T_{bi}(t). \quad (1)$$

In general, we will not explicitly include the bi and b subscripts.

B. Setup

We wish to estimate the continuous-time state of a continuum robot $\mathbf{x}(s, t)$ stochastically over both arclength (s) and time (t). We take a Bayesian inference approach by first defining a prior, then combining measurement data to estimate a posterior distribution for the robot state. We choose a state representation that includes a pose $T(s, t) \in SE(3)$, a body-centric strain $\epsilon(s, t) \in \mathbb{R}^6$, and body-centric velocity of the robot $\varpi(s, t) \in \mathbb{R}^6$.

$$\mathbf{x}(s, t) = \{T(s, t), \epsilon(s, t), \varpi(s, t)\} \quad (2)$$

While not strictly correct, we will often use $\mathbf{x}(s, t)$ as a vector throughout this work, an abuse of notation that will make later equations easier to follow. In a perfect world, we would want to be able to represent the prior for our state as a Gaussian process (GP) in closed-form over time and space,

$$\mathbf{x}(s, t) \sim \mathcal{GP}(\tilde{\mathbf{x}}(s, t), \tilde{\mathbf{P}}(s, s'; t, t')). \quad (3)$$

This work does not propose such a closed-form representation. Rather, we will approximate the prior through the construction and solution of a factor-graph optimization problem, relying heavily on analogy to the time and space systems presented in [36], [37]. Though this approach may leave the reader longing for a more thorough theoretical justification for the

validity of this prior, we will show that such approximations result in reasonable estimates in practice.

The derivation for our estimation framework begins with a continuum robot's kinematics. The basic kinematic expressions for a rod are given by [44], [45]

$$\frac{\partial T}{\partial t} = \varpi^\wedge T \quad (4a)$$

$$\frac{\partial T}{\partial s} = \epsilon^\wedge T \quad (4b)$$

$$\frac{\partial \varpi}{\partial s} = \frac{\partial \epsilon}{\partial t} + \epsilon^\wedge \varpi \quad (4c)$$

where $T \in SE(3)$ is a transformation matrix, $\varpi \in \mathbb{R}^6$ is the body-centric velocity, and $\epsilon \in \mathbb{R}^6$ is the body-centric strain. Note that each state variable still depends on s and t , we drop it here for conciseness. The last relation (4c) is a consistency constraint that relates the spatial and temporal derivatives of the body-centric velocity and strain.

C. Approximate Dynamics

At the core of our method is a significant simplification of a dynamic Cosserat-rod model made with the assumption that data will be available to compensate for modelling errors. This explicitly sets up our estimation problem as a tradeoff between computation time, prior accuracy, and posterior accuracy. To best illustrate this approximation, consider a dynamic model for a Cosserat rod. We choose to show a simple linear elastic, undamped, gravity-free Cosserat model [44], [45], though a more complex model would demonstrate a similar point. In our notation, these expressions are given by:

$$K \frac{\partial \epsilon}{\partial s} + \epsilon^\wedge K(\epsilon - \epsilon_0) + \mathbf{f} = M \frac{\partial \varpi}{\partial t} + \varpi^\wedge M \varpi. \quad (5)$$

Here, $K \in \mathbb{R}^{6 \times 6}$ is a positive-definite stiffness matrix, $M \in \mathbb{R}^{6 \times 6}$ is a positive-definite inertial matrix, $\mathbf{f} \in \mathbb{R}^6$ represents an external wrench, and $\epsilon_0 \in \mathbb{R}^6$ is the system strain at rest.

At this point, the system dynamics are usually solved using a numerical integration method [18], [45]. However, these approaches rely on having accurate information not only about the system's physical characteristics but also about the external loads applied. This works well enough in controlled environments but may not be sufficient for operation in more complex and possibly unknown environments. Following the work of [36], [37], we make a seemingly large approximation of the dynamics by injecting white noise onto the second-order derivative terms. We will later show that this approximation is reasonable given an appropriate selection of measurements. Specifically, we make the following 'white-noise-on-acceleration' (and the analogous 'white-noise-on-strain-rate') assumptions:

$$\begin{aligned} \frac{\partial \varpi}{\partial t} &= M^{-1} K \frac{\partial \epsilon}{\partial s} + M^{-1} \epsilon^\wedge K(\epsilon - \epsilon_0) \\ &\quad + M^{-1} \mathbf{f} - M^{-1} \varpi^\wedge M \varpi \\ &\approx \mathbf{w}_1, \\ \frac{\partial \epsilon}{\partial s} &= K^{-1} M \frac{\partial \varpi}{\partial t} + K^{-1} \varpi^\wedge M \varpi \\ &\quad - K^{-1} \epsilon^\wedge K(\epsilon - K^{-1} \epsilon_0) - K^{-1} \mathbf{f} \end{aligned} \quad (6a)$$

$$\approx \mathbf{w}_2, \quad (6b)$$

with noise terms defined as

$$\mathbf{w}_1(s, t) \sim \mathcal{GP}(\mathbf{0}, \mathbf{Q}_1 \delta(s - s') \delta(t - t')), \quad (6c)$$

$$\mathbf{w}_2(s, t) \sim \mathcal{GP}(\mathbf{0}, \mathbf{Q}_2 \delta(s - s') \delta(t - t')). \quad (6d)$$

Here we use a zero-mean Gaussian process white noise with power spectral density matrices $\mathbf{Q}_i \in \mathbb{R}^{6 \times 6}$. These are stochastic processes with each point in arclength and time (s, t) being uncorrelated to one another and having a probability density of \mathbf{Q}_i . Additionally, we inject noise on the cross-derivative terms while ensuring to maintain the consistency constraint. This gives us the following approximations:

$$\frac{\partial \epsilon}{\partial t} \approx \mathbf{w}_3, \quad (7a)$$

$$\frac{\partial \varpi}{\partial s} \approx \epsilon^\wedge \varpi + \mathbf{w}_3, \quad (7b)$$

with the noise term defined as

$$\mathbf{w}_3(s, t) \sim \mathcal{GP}(\mathbf{0}, \mathbf{Q}_3 \delta(s - s') \delta(t - t')). \quad (7c)$$

The approximate ‘dynamics’ as presented form the basis for our continuous-time estimation prior.

D. Prior Factors

We wish to construct a sum of prior factors that when minimized, provides a solution to the approximate dynamics presented in Section II-C. We will do this through the use of binary factors (connecting two states) in both time and space. Consider a discrete set of N points in arclength, s_1, s_2, \dots, s_N , and a discrete set of K points in time, t_1, t_2, \dots, t_K . These arclengths and times will mark a series of states that we will explicitly estimate and use in the following factors. Afterwards, we will show that we can interpolate between these states in time or space, resulting in a continuous state representation.

1) *Time Factors*: We begin by constructing a series of factors that relate the state at a specific point in time, t_k , to the state at some later point in time, t_{k+1} . Beginning with the time-dynamics of our state variables,

$$\frac{\partial \mathbf{T}}{\partial t} = \varpi^\wedge \mathbf{T}, \quad \frac{\partial \epsilon}{\partial t} \approx \mathbf{w}_3, \quad \frac{\partial \varpi}{\partial t} \approx \mathbf{w}_1, \quad (8a)$$

we can see that these expressions are exactly those of [37] in the time-only GP estimator method. In fact, the pose \mathbf{T} and velocity ϖ are directly analogous, with only the addition of the strain ϵ to the state vector. In the method of [37], the authors choose to introduce a local pose variable and apply a ‘white-noise-on-acceleration’ prior on the now linear state variables. This works well enough in the time-only and arclength-only cases, but the addition of the consistency constraint in (4c) makes this approach less suitable for our continuous-time estimation framework. Instead, we will construct full nonlinear factors, sacrificing the simplicity of the linearized factors in favor of a more general solution that can be applied to a problem that has arclength and time. Consider an Euler step to the expressions in (8), assuming constant strain

and velocity at some arbitrary arclength s_n , the mean of which is approximately given by

$$\bar{\mathbf{T}}(s_n, t_{k+1}) \approx \exp(\Delta t \bar{\varpi}(s_n, t_k)^\wedge) \bar{\mathbf{T}}(s_n, t_k), \quad (9a)$$

$$\bar{\epsilon}(s_n, t_{k+1}) \approx \bar{\epsilon}(s_n, t_k), \quad (9b)$$

$$\bar{\varpi}(s_n, t_{k+1}) \approx \bar{\varpi}(s_n, t_k). \quad (9c)$$

From here we wish to form an error term. A natural choice is to look at the difference between the state at time t_{k+1} and the state at time t_k propagated forward according to the approximate dynamics. This difference reflects a deviation from the approximate dynamics, which we wish to minimize. This error term is given by

$$\mathbf{e}_{\text{time}}^{(n,k)} = \begin{bmatrix} \ln(\bar{\mathbf{T}}_{n,k+1} \bar{\mathbf{T}}_{n,k}^{-1})^\vee - \Delta t \bar{\varpi}_{n,k} \\ \bar{\epsilon}_{n,k+1} - \bar{\epsilon}_{n,k} \\ \bar{\varpi}_{n,k+1} - \bar{\varpi}_{n,k} \end{bmatrix}. \quad (10)$$

With each of these terms, the error is zero when the state progresses in between time steps is exactly according to the approximate dynamic model. We wish to incorporate covariances between the state elements through the use of a weighted cost term. In previous works [36], [37], such weight matrices are determined through determining the uncertainty added to the system over a specific window of time (or arclength) by integrating the system’s differential equations, including a zero-mean GP white noise term. We will use the results from these works ‘by analogy’ for our factors, acknowledging that without a closed-form solution to the covariance of our prior, these approaches are not quite equivalent. In practice, however, we demonstrate the ability to tune the presented covariance terms in order to obtain a consistent estimator, pointing towards this approximation being reasonable. For the time factor, we approximate the symmetric covariance accumulation matrix as

$$\mathbf{Q}_t(\Delta t) = \begin{bmatrix} \frac{1}{3} \Delta t^3 \mathbf{Q}_1 & * & * \\ \mathbf{0} & \Delta t \mathbf{Q}_3 & * \\ \frac{1}{2} \Delta t^2 \mathbf{Q}_1 & \mathbf{0} & \Delta t \mathbf{Q}_1 \end{bmatrix}, \quad (11a)$$

$$\Delta t = t_{k+1} - t_k, \quad (11b)$$

an analogous form to that of [37], a fact that seems reasonable given the system setup. Armed with both the covariance accumulation matrix and a mean error expression, we can form a full weighted cost term, J

$$J_{\text{time}}^{(n,k)} = \frac{1}{2} \mathbf{e}_{\text{time}}^{(n,k)T} \mathbf{Q}_t(\Delta t)^{-1} \mathbf{e}_{\text{time}}^{(n,k)}. \quad (12)$$

2) *Arclength Factors*: We continue by constructing factors for the arclength parameter between states at two points in arclength, s_n and s_{n+1} , along the backbone of the robot. Beginning with the arclength dynamics of our state variables,

$$\frac{\partial \mathbf{T}}{\partial s} = \epsilon^\wedge \mathbf{T}, \quad \frac{\partial \epsilon}{\partial s} \approx \mathbf{w}_2, \quad \frac{\partial \varpi}{\partial s} \approx \epsilon^\wedge \varpi + \mathbf{w}_3. \quad (13)$$

Again, an Euler step is taken to approximate the mean of the state variables along a progression in arclength. The mean of the state variables is approximately given by

$$\bar{\mathbf{T}}(s_{n+1}, t) \approx \exp(\Delta s \bar{\epsilon}(s_n, t)^\wedge) \bar{\mathbf{T}}(s_n, t) \quad (14a)$$

$$\bar{\epsilon}(s_{n+1}, t) \approx \bar{\epsilon}(s_n, t) \quad (14b)$$

$$\bar{\omega}(s_{n+1}, t) \approx \bar{\omega}(s_n, t) + \Delta s \epsilon(s_n, t)^\wedge \bar{\omega}(s_n, t). \quad (14c)$$

As before, we can construct the following spatial error expressions for a specific time t_k :

$$e_{\text{space}}^{(n,k)} = \begin{bmatrix} \ln(\bar{T}_{n+1,k} \bar{T}_{n,k}^{-1})^\vee - \Delta s \epsilon_{n,k} \\ \bar{\epsilon}_{n+1,k} - \bar{\epsilon}_{n,k} \\ \bar{\omega}_{n+1,k} - \bar{\omega}_{n,k} - \Delta s \epsilon_{n,k}^\wedge \bar{\omega}_{n,k} \end{bmatrix}, \quad (15)$$

with these terms again equalling zero when the states progress according to the arclength dynamics model. The covariance accumulation matrix for this factor is not as easy to draw by analogy to existing works because of the nonlinear consistency constraint term. In this case, we linearize the term and integrate over space to achieve an approximation for the symmetric covariance accumulation matrix that we need

$$Q_s^{(k)}(\Delta s) = \begin{bmatrix} \frac{1}{3} \Delta s^3 Q_2 & * & * \\ \frac{1}{2} \Delta s^2 Q_1 & \Delta s Q_1 & * \\ -\frac{1}{3} \Delta s^3 W^* & -\frac{1}{2} \Delta s^2 W^* & Q^* \end{bmatrix}, \quad (16a)$$

$$W^* = \varpi_{n,k}^\wedge Q_2, \quad (16b)$$

$$Q^* = \Delta s Q_3 + \frac{1}{3} \Delta s^3 \varpi_{n,k}^\wedge Q_2 \varpi_{n,k}^T, \quad (16c)$$

$$\Delta s = s_{n+1} - s_n. \quad (16d)$$

In contrast to the time case, $Q_s^{(k)}$ depends on the state variable $\varpi(s_n, t_k)$, a fact that follows from the nonlinear term in the consistency constraint. The top left elements of this matrix unsurprisingly echo the result of [36], with the remaining terms dealing with the new velocity component of the state. We can again form a full weighted cost term,

$$J_{\text{space}}^{(n,k)} = \frac{1}{2} e_{\text{space}}^{(n,k)T} Q_s^{(k)}(\Delta s)^{-1} e_{\text{space}}^{(n,k)}. \quad (17)$$

A subtle assumption being made in this process is that the noise modelling the change of strain over time $\frac{\partial \epsilon}{\partial t}$ in this arclength factor is different to the noise modelling the change of velocity over arclength $\frac{\partial \varpi}{\partial s}$. The consistency constraint says that these should, in fact, be related; however, given the terms as defined, there is nothing enforcing such a relationship. As written we are treating these terms as two independent samples from the same distribution. This choice has many practical benefits, such as simplifying the problem sparsity by removing a correlation term between the spatial and temporal errors and improving numerical stability. This decision will ultimately not greatly affect the performance of the estimator.

3) *Unary Factors*: A third type of factor that we wish to include, which is not novel to this work, but is included for completeness, are unary factors. Unary factors are used to represent the prior knowledge of the system at a specific point in arclength and time. These factors are typically used to represent the initial state, or any other prior knowledge that is known about the system. In the case of continuum robots, these factors can be used to represent information we may have about the base of the robot (e.g., the robot is stationary), the tip (e.g., the strain is zero), or any number of places along the body at any point in time (e.g., the robot is known to pass through a narrow opening). In this work, rather than locking the base state as done in [36], [37], we provide a full unary factor at the robot base at each timestep as a

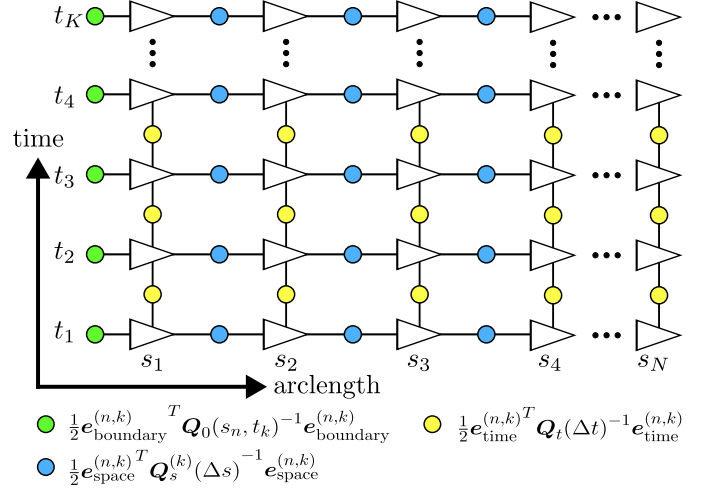


Fig. 2. Factor-graph representation of the prior for the continuous-time estimation framework. Unary factors are depicted using green dots, binary space factors are represented with blue dots, and binary time factors are depicted using yellow dots. Each triangle represents a node at a specific point in arclength and time that is estimated directly in our solver. Each factor is connected to one or two nodes, and never between two nodes that vary in both arclength and time.

boundary condition. This approach should more closely reflect the physical reality of a base-mounted CR that may experience small disturbances in its mounting during operation.

Such a factor assumes that we have some external guess (or just as easily a direct measurement) for the state of the robot $x_0(s, t)$ that represents the actual state corrupted by some noise. Specifically, given an estimate for the state variables at a given arclength s and time t , we assume that the estimate is related to the true state via

$$x_0(s, t) = \begin{bmatrix} T_0(s, t) \\ \epsilon_0(s, t) \\ \varpi_0(s, t) \end{bmatrix} \sim \mathcal{N}(x(s, t), Q_0(s, t)).$$

We define an error term for such a factor as

$$e_{\text{boundary}}^{(n,k)} = \begin{bmatrix} \ln(\bar{T}_0(s_n, t_k) \bar{T}(s_n, t_k)^{-1})^\vee \\ \bar{\epsilon}_0(s_n, t_k) - \bar{\epsilon}(s_n, t_k) \\ \bar{\varpi}_0(s_n, t_k) - \bar{\varpi}(s_n, t_k) \end{bmatrix}. \quad (18)$$

In scenarios where information is only known about part of the state a subset of this error term may be used (e.g., the tip strain is known but not the pose or velocity). This term has a cost contribution of

$$J_{\text{boundary}}^{(n,k)} = \frac{1}{2} e_{\text{boundary}}^{(n,k)T} Q_0(s_n, t_k)^{-1} e_{\text{boundary}}^{(n,k)}. \quad (19)$$

4) *Factor Graph*: With each of the three factors introduced, a full factor graph for the prior can be constructed. When thinking about where to assemble specific factors, it is important to remember what the factors are: an Euler approximation for the approximate dynamics of the system. The continuous PDEs presented in (8) and (13) are theoretically smooth, where, when integrating over arclength and time, the path taken should not matter. Unfortunately, this does not hold true when making Euler approximations. The factor-graph construction should therefore not prefer one integration path

over another. A natural choice is to make a grid of nodes across arclength and time, with unary factors used to apply initial or boundary conditions. This approach is taken and depicted in Fig. 2. A grid is assembled using N points in space and K points in time. The nodes of this grid represent states at specific arclengths and times that will be explicitly estimated by the estimator. A boundary condition is applied along the $s = 0$ boundary, corresponding to the physical base of the robot. This results in a factor graph with NK estimation nodes and $N(2K - 1)$ factors. As each node in this graph is only connected to its immediate neighbours, an inherent sparsity is introduced, a fact that is explored further in Section II-G.

E. Measurement Factors

We wish to include noisy measurements from multiple sensors and modalities in this framework. These include direct pose measurements from an electromagnetic pose tracker and rotation rates from a gyroscope. Both of these modalities can be quickly included in our framework, given a measurement model that relates the sensor measurement to the state variables $\mathbf{x}(s_n, t_k)$. The following sections will present such models for each of these modalities.

1) *Pose Measurements*: We assume that we can take direct pose measurements at a specific arclength down the robot, s , at a specific point in time, t . Let $\tilde{\mathbf{T}}$ represent such a measurement. Following [36], [43], [46], we assume this pose measurement is drawn from a Gaussian with a mean at the true pose, and some zero-mean sensor noise.

$$\tilde{\mathbf{T}} = \exp(\mathbf{n}^\wedge) \mathbf{T}(s, t), \quad \mathbf{n} \sim \mathcal{N}(\mathbf{0}, \mathbf{R}_{\text{pose}}), \quad (20)$$

where \mathbf{R}_{pose} is the covariance of the pose sensor noise. Using this setup, we define a measurement error term as the difference between the predicted pose and the actual pose measurement, expressed in the Lie algebra as

$$\mathbf{e}_{\text{pose}} = \ln(\tilde{\mathbf{T}} \mathbf{T}(s, t)^{-1})^\vee. \quad (21)$$

The total cost associated with a pose measurement is then given by

$$J_{\text{pose}} = \frac{1}{2} \mathbf{e}_{\text{pose}}^T \mathbf{R}_{\text{pose}}^{-1} \mathbf{e}_{\text{pose}}. \quad (22)$$

representing the negative log likelihood of the pose measurement.

2) *Gyro Measurements*: We assume again that we can take direct measurements of the angular velocity at a specific arclength down the robot, s , at a specific point in time, t . Let $\tilde{\boldsymbol{\omega}}$ represent such a measurement. We assume this measurement is drawn from a Gaussian with a mean at the true angular velocity, and some zero-mean sensor noise

$$\tilde{\boldsymbol{\omega}} = \boldsymbol{\omega}(s, t) + \mathbf{n}, \quad \mathbf{n} \sim \mathcal{N}(\mathbf{0}, \mathbf{R}_{\text{gyro}}), \quad (23)$$

where \mathbf{R}_{gyro} is the covariance of the gyroscope sensor noise. Noting that the linear velocity, \mathbf{v} , and angular velocity, $\boldsymbol{\omega}$, is included in our state via $\boldsymbol{\varpi} = \begin{bmatrix} \mathbf{v} \\ \boldsymbol{\omega} \end{bmatrix}$. The error term is then given as

$$\mathbf{e}_{\text{gyro}} = \tilde{\boldsymbol{\omega}} - \boldsymbol{\omega}(s, t), \quad (24)$$

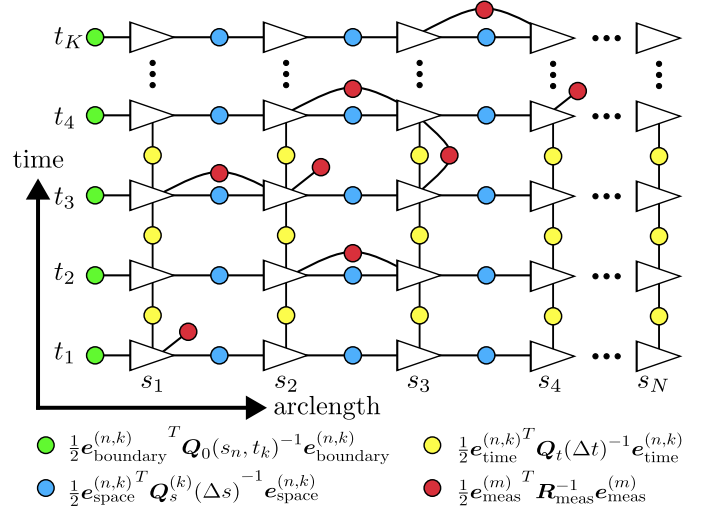


Fig. 3. Factor graph representation of the full continuous-time estimation framework. Unary factors are depicted using green dots, binary space factors with blue dots, and binary time factors with yellow dots. Each triangle represents a node at a specific point in arclength and time that is estimated directly in our solver. Measurements are added sparsely either directly to an estimation node or as an interpolated factor between two estimation nodes and are depicted as red dots. In practice, measurements will solely be added as interpolated factors in time, as the spatial estimation points included in the graph will be selected to align with the physical placement of each sensor on the robot.

with a total cost given by

$$J_{\text{gyro}} = \frac{1}{2} \mathbf{e}_{\text{gyro}}^T \mathbf{R}_{\text{gyro}}^{-1} \mathbf{e}_{\text{gyro}}. \quad (25)$$

While we have presented measurement models for pose and gyroscope sensors, the framework is general enough to include other sensor modalities provided they have a sensor model that relates the measurement to the state variables in $\mathbf{x}(s, t)$ and a known Jacobian. Fiber Bragg Grating Sensor [36], strain gauges [40], and stereo cameras [37] have been included in similar frameworks in past works.

F. Interpolation

In the previous section, the measurement models require access to the state at a specific arclength and time, $\mathbf{x}(s, t)$. In practice, we wish to only perform estimation on a discrete set of states $\{\mathbf{x}(s_n, t_k)\}_{n \in \{1, \dots, N\}, k \in \{1, \dots, K\}}$. While it may be reasonable to assume that the arclength of a sensor measurement is included in this set, as sensors are typically fixed at specific locations along the robot, the same cannot be said for the time component. As we wish to include sensors that produce asynchronous measurements with inconsistent timestamps, an interpolation scheme is required.

1) *Interpolation in Time*: Looking at time in isolation reveals a very similar formulation to that of [37]. This similarity, we argue, is close enough to allow us to use the same interpolation scheme as presented in [37]; we will validate this with the results in Section IV-D. Specifically, we interpolate in time using

$$\boldsymbol{\gamma}_{n,k}(s, t) = [\boldsymbol{\Lambda}_t(s, t) \quad \boldsymbol{\Psi}_t(s, t)] \begin{bmatrix} \boldsymbol{\gamma}_{n,k}(s, t_k) \\ \boldsymbol{\gamma}_{n,k}(s, t_{k+1}) \end{bmatrix}, \quad (26a)$$

$$\Psi_t(s, t) = \mathbf{Q}_t(\tau - t_k) \Phi_t(t_{k+1} - \tau) \mathbf{Q}_t(t_{k+1} - t_k)^{-1}, \quad (26b)$$

$$\Lambda_t(s, t) = \Phi_t(\tau - t_k) - \Psi_t(s, t) \Phi_t(t_{k+1} - t_k), \quad (26c)$$

$$\Phi_t(\Delta t) = \begin{bmatrix} \mathbf{I} & \mathbf{0} & \Delta t \mathbf{I} \\ \mathbf{0} & \mathbf{I} & \mathbf{0} \\ \mathbf{0} & \mathbf{0} & \mathbf{I} \end{bmatrix}, \quad (26d)$$

where we use a local coordinate, $\gamma_{n,k}$, defined as

$$\gamma_{n,k}(s, t) = \begin{bmatrix} \xi_{n,k}(s, t) \\ \frac{\partial}{\partial s} \xi_{n,k}(s, t) \\ \frac{\partial}{\partial t} \xi_{n,k}(s, t) \end{bmatrix}, \quad (27a)$$

$$\xi_{n,k}(s, t) = \ln \left(\mathbf{T}(s, t) \mathbf{T}(s_n, t_k)^{-1} \right)^\vee, \quad (27b)$$

$$\frac{\partial}{\partial s} \xi_{n,k}(s, t) = \mathcal{J}(\xi_{n,k}(s, t))^{-1} \epsilon(s, t), \quad (27c)$$

$$\frac{\partial}{\partial t} \xi_{n,k}(s, t) = \mathcal{J}(\xi_{n,k}(s, t))^{-1} \varpi(s, t), \quad (27d)$$

with

$$s_n \leq s \leq s_{n+1}, \quad (27e)$$

$$t_k \leq t \leq t_{k+1}. \quad (27f)$$

The interpolated state variables can then be expressed as

$$\begin{aligned} \mathbf{x}(s, t) &= \mathbf{f}(\mathbf{x}_{n,k}, \mathbf{x}_{n,k+1}) \\ &= \left\{ \begin{array}{l} \exp(\xi_{n,k}(s, t)^\wedge) \mathbf{T}(s_n, t_k) \\ \mathcal{J}(\xi_{n,k}(s, t)) \frac{\partial}{\partial s} \xi_{n,k}(s, t) \\ \mathcal{J}(\xi_{n,k}(s, t)) \frac{\partial}{\partial t} \xi_{n,k}(s, t) \end{array} \right\}. \end{aligned} \quad (28)$$

Covariance interpolation happens after the main solve making use of the Laplace approximation. We can solve for interpolated covariances with

$$\begin{aligned} \hat{\mathbf{P}}(s, t) &= \check{\mathbf{P}}(s, t) + [\Lambda_t(s, t) \quad \Psi_t(s, t)] \mathbf{P}_{n,k}^{(t)} \begin{bmatrix} \Lambda_t^T(s, t) \\ \Psi_t^T(s, t) \end{bmatrix}, \\ \mathbf{P}_{n,k}^{(t)} &= \begin{bmatrix} \mathbf{P}_{n,k;n,k} & \mathbf{P}_{n,k;n,k+1} \\ \mathbf{P}_{n,k+1;n,k} & \mathbf{P}_{n,k+1;n,k+1} \end{bmatrix}. \end{aligned} \quad (29)$$

2) *Interpolation in Space:* We use the same interpolation scheme as presented in [36]. The approximation being made here is that of the consistency constraint in (13), approximating it as

$$\frac{\partial \varpi}{\partial s} \approx \epsilon^\wedge \varpi + \mathbf{w}_3 \approx \mathbf{w}_3. \quad (30)$$

This approximation results in this scheme performing linear interpolation on the velocity component along arclength (as opposed to the spline interpolation for pose.) From here, interpolation along arclength of the estimator is achieved using the same formulation as the time-only interpolation as worked through in the previous section.

3) *Interpolation of Measurement Factors:* In order to include continuous-time measurements in our factor graph, we must be able to construct Jacobians to the measurement models for the states that are included in the graph. To do this, we make use of the interpolation Jacobians and the chain rule. Specifically, given a measurement model $\mathbf{y}(s, t) = \mathbf{g}(\mathbf{x}(s, t)) + \mathbf{n}$ and a time interpolation model $\mathbf{x}(s_n, t) = \mathbf{f}(\mathbf{x}(s_n, t_k), \mathbf{x}(s_n, t_{k+1})) + \mathbf{w}$, we can construct the Jacobian of the measurement model with respect to the state variables

at a specific arclength and times, $\mathbf{x}(s_n, t_k), \mathbf{x}(s_n, t_{k+1})$, as follows:

$$\begin{aligned} \mathbf{y}(s, t) &\approx \bar{\mathbf{y}}(s, t) + \mathbf{n} + \mathbf{G}|_{\bar{\mathbf{x}}(s, t)} \delta \mathbf{x}(s, t) \\ &= \bar{\mathbf{y}}(s, t) + \underbrace{\mathbf{n} + \mathbf{G}|_{\bar{\mathbf{x}}(s, t)} \mathbf{w}(s, t)}_{\mathbf{n}_i} \\ &\quad + \mathbf{G}|_{\bar{\mathbf{x}}(s, t)} \mathbf{F}|_{\bar{\mathbf{x}}_{n,k}, \bar{\mathbf{x}}_{n,k+1}} \begin{bmatrix} \delta \mathbf{x}_{n,k} \\ \delta \mathbf{x}_{n,k+1} \end{bmatrix}, \end{aligned} \quad (31a)$$

$$\mathbf{n}_i \sim \mathcal{N}(\mathbf{0}, \mathbf{R} + \mathbf{G}|_{\bar{\mathbf{x}}(s, t)} \mathbf{Q}_\tau \mathbf{G}|_{\bar{\mathbf{x}}(s, t)}^T), \quad (31b)$$

where $\mathbf{G}|_{\bar{\mathbf{x}}(s, t)}$ is the measurement model Jacobian evaluated at the interpolated state variables and $\mathbf{F}|_{\bar{\mathbf{x}}_{n,k}, \bar{\mathbf{x}}_{n,k+1}}$ is the interpolation model Jacobian evaluated at the surrounding states. The details for these Jacobians can be found in Appendix B. This formulation allows us to include measurements at any point in time in the estimation problem as long as it is within the estimation window. Fig. 3 shows a factor graph representing such an application of interpolated measurements. It is worth mentioning that this approach implicitly makes an assumption that the interpolated states between two estimation nodes are independent of each other. This has the effect of multiple measurements contributing to overconfidence, with the effect being minimized with smaller choices of Δt . We find that with most practical choices for Δt , reasonable estimates are still produced, a result similarly demonstrated in other works making use of the same approximation [36], [37]. Section IV-D explores the ramifications of this assumption in more detail.

G. Solver

The total cost function for the factor graph is given by the sum of the prior and measurement costs. Specifically, we have the following cost terms for the prior and measurements:

$$J_p = \sum_n \sum_k J_{\text{space}}^{(n,k)} + J_{\text{time}}^{(n,k)} + J_{\text{boundary}}^{(n,k)}, \quad (32a)$$

$$J_m = \sum_m J_{\text{pose / gyro}}^{(m)}. \quad (32b)$$

Now we face the challenge of minimizing the cost. Our optimization problem is

$$\mathbf{x}^* = \arg \min_{\mathbf{x}} J_p(\mathbf{x}) + J_m(\mathbf{x}) \quad (33a)$$

where

$$\mathbf{x} = \begin{bmatrix} \mathbf{x}_{1,1} \\ \mathbf{x}_{2,1} \\ \vdots \\ \mathbf{x}_{N,K} \end{bmatrix}. \quad (33b)$$

The state \mathbf{x}^* is then the robot configuration that minimizes the cost function, and is an approximate solution to the dynamics presented in Section II-C. In order to solve this problem we will first linearize the cost term and then use a Gauss-Newton solver to find the solution iteratively. The state is perturbed in an $SE(3)$ -sensitive way about an operating point in the same manner as [36], [37];

$$\mathbf{T}_{n,k} = \exp(\delta \mathbf{t}_{n,k}^\wedge) \mathbf{T}_{\text{op}}^{(n,k)}, \quad (34a)$$

$$\epsilon_{n,k} = \epsilon_{\text{op}}^{(n,k)} + \delta\epsilon_{n,k}, \quad (34b)$$

$$\varpi_{n,k} = \varpi_{\text{op}}^{(n,k)} + \delta\varpi_{n,k}. \quad (34c)$$

It will be practical to define a shorthand through a slight abuse of notation,

$$\mathbf{x}_{n,k} = \mathbf{x}_{\text{op}}^{(n,k)} + \delta\mathbf{x}_{n,k}, \quad \delta\mathbf{x}_{n,k} = \begin{bmatrix} \delta\mathbf{t}_{n,k} \\ \delta\epsilon_{n,k} \\ \delta\varpi_{n,k} \end{bmatrix}. \quad (35)$$

We assemble the perturbed state vector into a stacked vector

$$\mathbf{x} = \mathbf{x}_{\text{op}} + \delta\mathbf{x}, \quad \delta\mathbf{x} = \begin{bmatrix} \delta\mathbf{x}_{1,1} \\ \delta\mathbf{x}_{2,1} \\ \vdots \\ \delta\mathbf{x}_{N,K} \end{bmatrix}. \quad (36)$$

We can now rewrite our cost function in a form similar to that of [36], [43], removing the need for summations:

$$J = \frac{1}{2} \mathbf{e}_p^T \mathbf{Q}^{-1} \mathbf{e}_p + \frac{1}{2} \mathbf{e}_m^T \mathbf{R}^{-1} \mathbf{e}_m, \quad (37)$$

where

$$\mathbf{e}_p = \begin{bmatrix} \mathbf{e}_p^{(1)} \\ \mathbf{e}_p^{(2)} \\ \vdots \\ \mathbf{e}_p^{(N(2K-1))} \end{bmatrix}, \quad \mathbf{Q} = \text{diag}\{\mathbf{Q}^{(1)}, \dots, \mathbf{Q}^{(N(2K-1))}\}, \quad (38)$$

where each $\mathbf{e}_p^{(i)}$ and $\mathbf{Q}^{(i)}$ term corresponds to the error and covariance vector of one of the $N(2K-1)$ prior factors. The ordering does not particularly matter in this case. Further,

$$\mathbf{e}_m = \begin{bmatrix} \mathbf{e}_m^{(1)} \\ \mathbf{e}_m^{(2)} \\ \vdots \\ \mathbf{e}_m^{(M)} \end{bmatrix}, \quad \mathbf{R} = \text{diag}\{\mathbf{R}^{(1)}, \dots, \mathbf{R}^{(M)}\}, \quad (39)$$

where each $\mathbf{e}_m^{(i)}$ and $\mathbf{R}^{(i)}$ term corresponds to the error and covariance vector of one of M measurement factors. Using the perturbations from Equation (34) and linearizing the error terms, we get

$$\mathbf{e}_p = \mathbf{e}_{p,\text{op}} + \mathbf{E}_p \delta\mathbf{x}, \quad (40a)$$

$$\mathbf{e}_m = \mathbf{e}_{m,\text{op}} + \mathbf{E}_m \delta\mathbf{x}, \quad (40b)$$

where \mathbf{E}_p and \mathbf{E}_m are the Jacobian matrices of the prior and measurement error terms, respectively. The details of all Jacobians can be found in Appendix B. The total cost function can then be written as

$$J \approx \frac{1}{2} (\mathbf{e}_{p,\text{op}} + \mathbf{E}_p \delta\mathbf{x})^T \mathbf{Q}^{-1} (\mathbf{e}_{p,\text{op}} + \mathbf{E}_p \delta\mathbf{x}) + \frac{1}{2} (\mathbf{e}_{m,\text{op}} + \mathbf{E}_m \delta\mathbf{x})^T \mathbf{R}^{-1} (\mathbf{e}_{m,\text{op}} + \mathbf{E}_m \delta\mathbf{x}). \quad (41)$$

The minimizing solution to this cost function can be found as the solution to

$$\begin{aligned} & \left(\mathbf{E}_p^T \mathbf{Q}^{-1} \mathbf{E}_p + \mathbf{E}_m^T \mathbf{R}^{-1} \mathbf{E}_m \right) \delta\mathbf{x}^* \\ &= - \left(\mathbf{E}_p^T \mathbf{Q}^{-1} \mathbf{e}_{p,\text{op}} + \mathbf{E}_m^T \mathbf{R}^{-1} \mathbf{e}_{m,\text{op}} \right). \end{aligned} \quad (42)$$

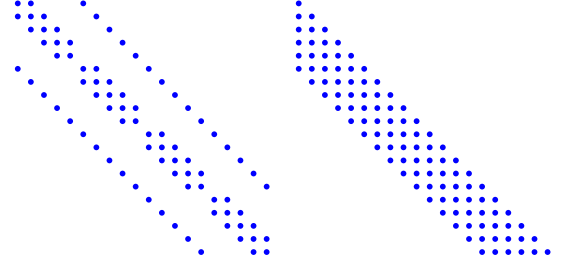


Fig. 4. Sparsity structure of the problem's inverse Kernel matrix $\tilde{\mathbf{P}}^{-1}$ (left) and its associated Cholesky factor $\tilde{\mathbf{L}}$ (right) for a estimation problem with $N = 5$, $K = 4$. The sparsity structure follows from the factor graph in Fig. 2. Each row and column of the matrix corresponds to a node in the factor graph, with each non-zero entry corresponding to a correlation between two nodes. The Cholesky factor is lower triangular, with non-zero entries bounded about the diagonal. The band scales with N , the number of spatial nodes in our state, leading to a solve complexity of $O(N^3 K)$, where K is the number of time steps in our estimation window. Given M measurements, the total system time complexity, including matrix construction, becomes $O(N^3 K + M)$.

The left-hand side of this expression is of note because of its specific sparsity structure shown in Fig. 4. By stacking the state in the order of (33b), we recover a banded structure with a band width that scales with the number of spatial nodes N in our state. Such a matrix can be solved efficiently using a Cholesky factorization, leading to a total solve complexity of $O(N^3 K)$, where K is the number of time steps in our estimation window. Including the cost of matrix construction, the total time complexity of computing the posterior is $O(N^3 K + M)$ where M is the number of measurements included. The proposed solver remains linear in time (K), a fact that is important for real-time applications.

As this system is a linearized approximation to the solution of the nonlinear problem, it is solved iteratively. The state is updated with the perturbation,

$$\mathbf{T}_{\text{op}}(s, t) \leftarrow \exp(\delta\mathbf{t}^*(s, t)^\wedge) \mathbf{T}_{\text{op}}(s, t), \quad (43a)$$

$$\epsilon_{\text{op}}(s, t) \leftarrow \epsilon_{\text{op}}(s, t) + \delta\epsilon^*(s, t), \quad (43b)$$

$$\varpi_{\text{op}}(s, t) \leftarrow \varpi_{\text{op}}(s, t) + \delta\varpi^*(s, t) \quad (43c)$$

and the process is repeated until convergence. The optimization process is terminated when the magnitude of the perturbation vector is sufficiently small,

$$\|\delta\mathbf{x}^*\| < \epsilon_{\text{tol}}, \quad (44)$$

or a maximum number of iterations is reached. On the final iteration, we use the Laplace approximation on the left side of the system, forming an approximation for the inverse covariance of the posterior state estimate,

$$\mathbf{P}^{-1} = \mathbf{E}_p^T \mathbf{Q}_p^{-1} \mathbf{E}_p + \mathbf{E}_m^T \mathbf{R}^{-1} \mathbf{E}_m. \quad (45)$$

The covariance may be extracted by taking advantage of the sparsity structure of the information matrix; we use the method from [47] to solve for relevant covariances in $O(N^3 K)$ time. Relevant covariances include the variance of each state variable, as well as its correlation to each state variable connected to it in the factor graph. As evident from the setup, our estimator is a batch solver. We leave non-batch filter-based extensions as future work, but note that the sparsity structure of the problem should lend itself well to such an approach.

III. APPARATUS

A. Simulation

We use a quasi-static simulator to validate our method on an extensible continuum robot. The static solver implemented is based on the quasi-static model from [44]. We simulate a three-segment TDCR that is fully extensible, which is to say, each of the segments can span from 0 to a full length of $\frac{1}{3}$ and back to 0. The robot has a length of 1 and has a trajectory of duration 1, both unitless values. The robot is actuated using three tendons per segment. Noisy pose measurements are simulated using a set of pose sensors placed at the tip of each segment. The pose measurements \tilde{T}_m are corrupted by Gaussian white noise \mathbf{n} on $SE(3)$, such that

$$\begin{aligned}\tilde{T}_m &\approx \exp(\mathbf{n}_m^\wedge) \tilde{T}_m, \\ \mathbf{n}_m &\sim \mathcal{N}(\mathbf{0}, \mathbf{R}), \\ \mathbf{R} &= \text{diag}\{5.00 \times 10^{-6}, 5.00 \times 10^{-6}, 5.00 \times 10^{-6}, \\ &\quad 1.25 \times 10^{-4}, 1.25 \times 10^{-4}, 1.25 \times 10^{-4}\}. \quad (46)\end{aligned}$$

The ‘Extensible’ trajectory sees this robot in a fully extended and bent state, contract fully to 0 length, and then extend to a new fully extended state. The extension part of this trajectory is shown in Fig. 6.

B. Prototype

We validate our method on a two-segment CR, the details of which are described in this section. The robot is designed to be a testbed for state estimation methods, and sacrifices size and weight for a number of sensors, enabling a ground truth comparison for the estimator.

1) *Robot Design*: The robot prototype is an inverted CR with a hollow nitinol backbone, which limits elongation and contraction. Additional PLA 3D printed modules [48] are used to increase the bending stiffness, with five resin 3D printed disks used to mount sensors and motion capture markers. The robot is 466mm long, 36mm in diameter, and consists of two actuated segments. Each segment is actuated using two opposing tendons.

2) *Sensors*: The prototype robot is equipped with nine sensors of three different types. There are five motion capture frames for the Vicon motion capture system (Vicon Motion Systems Ltd., UK) centered on the backbone of the robot, evenly spaced down the length of the robot. This system serves as a ground truth for the robot’s pose, providing $\sim 1\text{mm}$ position accuracy and $\sim 0.01\text{rad}$ rotational accuracy throughout operation at a rate of 15Hz. Two 6-degree-of-freedom (DoF) electromagnetic pose sensors (Aurora v3, Northern Digital Inc., Canada) are mounted on the robot, one at the tip and one at the base. Each collect data at 50Hz. Lastly, two 3DoF gyroscopes (ISM330DHCX, STMicroelectronics NV, Netherlands) are mounted at the tip and midpoint of the robot, each collecting data at a rate of 30Hz. Fig. 5 shows the robot prototype and sensor placements.

3) *Post-Processing*: Data collected from the sensors is processed after collection and before running the estimator. Outlier rejection and time synchronization of each data type

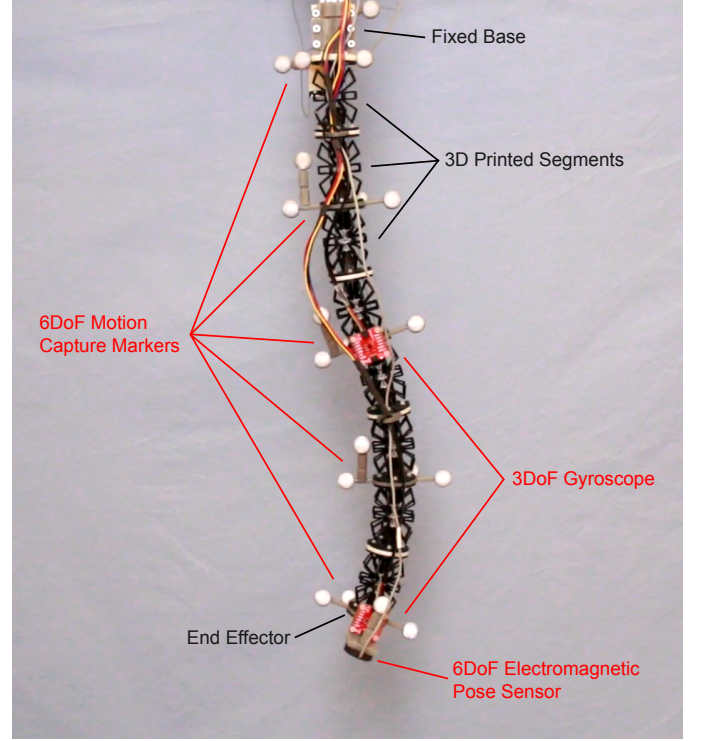


Fig. 5. Picture of the robot prototype described in Section III-B during data collection. Sensor locations are labelled in red with other relevant parts labelled in black.

are performed manually. Several static transforms in the system are required for comparing pose estimates to the ground truth data and are determined through hand-eye calibration. We define the following frames:

- v: Vicon world frame
- a: Aurora world frame
- g: Vicon frame fixed to the Aurora field generator
- m: Aurora base marker frame
- t: Aurora tip marker frame
- b: Base frame of the robot
- e: End-effector frame of the robot

Three unknown static transforms are needed in order to project measured frames into a ground-truth frame: T_{mb}, T_{te}, T_{ag} . We collect pose measurement data for calibration from the robot positioned statically in eight different configurations,

$$\mathcal{D} = \{\tilde{T}_{am}^{(1)}, \dots, \tilde{T}_{am}^{(N_1)}, \tilde{T}_{at}^{(1)}, \dots, \tilde{T}_{at}^{(N_2)}, \tilde{T}_{vb}^{(1)}, \dots, \tilde{T}_{vb}^{(N_3)}, \tilde{T}_{ve}^{(1)}, \dots, \tilde{T}_{ve}^{(N_4)}\}. \quad (47)$$

The unknown transforms T_{mb}, T_{te} and T_{ag} are then found directly using world-hand-eye calibration on this calibration dataset, we choose to use the method from [49]. In practice, we see an average reprojection errors between these two systems in our setup of $\sim 5\text{mm}$; this ends up contributing significantly to the overall reported errors of the estimator.

C. Estimator Parameters

This estimation framework gives the user the ability to tune the process noise and measurement noise parameters. The

measurement noise terms \mathbf{R}_i can be determined initially by the sensor characteristics and adjusted accordingly to achieve the desired estimator performance. We find that tuning these values to represent a slightly noisier sensor than what is observed aids in generating a consistent estimate. This likely comes from the assumption discussed in Section II-F3, tending to make estimates overconfident.

The remaining tunable parameters are the process noise matrices \mathbf{Q}_i . These should correspond to the uncertainty expected to be acquired along each of the relevant state dimensions. For example, to model a Kirchhoff rod, it is expected that the strain in the shearing and elongation dimensions is near zero, while the bending strains and twist account for most of the motion of the robot. As such, one could set the shearing strain values of $\mathbf{Q}_0, \mathbf{Q}_2, \mathbf{Q}_3$ to be low, corresponding to high certainty in the initial shear strain estimate, as well as high certainty in the shear strain not changing over arclength or time. In this way, the choice of these parameters fully determines the behaviour of the estimator. Each robot should be tuned individually to achieve the desired estimator behaviour and performance. All parameters used for both the prototype and the simulated robot estimators in this paper are provided in Appendix C.

For each experiment trajectory, the estimator discretizes the problem using $N = 17$ spatial nodes (or in simulation, $N = 19$, to ensure node placement spatially on the three-segment sensors) and places time nodes at a rate of 30Hz. The convergence threshold is set to $\epsilon_{\text{tol}} = 0.1$. This selection results in solve runtimes for the mean solution that are approximately ‘real-time’ (i.e., the estimator solves a 10s batch problem in under 10s). Explicit covariance estimation after the solve is optional and adds overhead, resulting in slower than real-time solves at the same rate and spatial discretization. All experiments are run on a laptop with an Intel i7-13850HX processor and 64 GB of RAM.

D. Benchmarks

We wish to compare our method to the GP method proposed in [36]. In fact, if we restrict our method to only use a value of $K = 1$ and drop the velocity component of the state, our method closely approximates the quasi-static approach. To ensure a fair comparison, we use the same process noise and measurement noise parameters as our method uses in only the spatial dimension. To compare the two methods, only pose measurements are used, as gyro-rates cannot be incorporated into a quasi-static method.

E. Error Metrics

To evaluate the performance of the estimator, we report three error metrics. As only 6DoF pose information is available as a ground truth, we report errors on position and orientation of the estimator and not on the velocity and strains. Ground truth data is collected from the Vicon motion capture system asynchronously. During evaluation, the estimator is queried at the same time steps as the ground truth data to avoid time alignment errors.

1) *Estimator Consistency*: First, the consistency of our estimator is evaluated using the average Normalized Estimation Error Squared (NEES) metric [43]. This metric is used to evaluate the consistency of the covariance estimates produced by the estimator. The average NEES for a given trajectory is computed as follows:

$$\mathbf{e}_n = \ln(\tilde{\mathbf{T}}_n \mathbf{T}_n^{-1})^\vee, \quad (48a)$$

$$d_{\text{NEES}} = \frac{1}{N} \sum_n \mathbf{e}_n^T \mathbf{P}_n^{-1} \mathbf{e}_n. \quad (48b)$$

Given we are using 6DoF pose information, a consistent estimator should produce an average NEES value of 6. A value greater than 6 indicates that the estimator is overconfident in its estimates, while a value less than 6 indicates that the estimator is underconfident.

2) *Pose Accuracy*: In many practical applications of continuum robots, the tip pose is of primary interest. To remain consistent with the CR literature [4], [13], [16], we report the accuracy of the tip pose using a mean distance metric at the tip of the robot. The position and orientation MAE are computed as follows:

$$d_{\text{MAE, pos}} = \frac{1}{N} \sum_{n=1}^N \frac{\|\tilde{\mathbf{p}}_n - \mathbf{p}_n\|_2}{L}, \quad (49a)$$

$$d_{\text{MAE, rot}} = \frac{1}{N} \sum_{n=1}^N \|\ln(\tilde{\mathbf{R}}_n \mathbf{R}_n^{-1})^\vee\|_2. \quad (49b)$$

We similarly present the body pose errors using the same metrics averaged over the four motion capture frames along the length of the robot that coincide with a non-zero length. We also present the root mean square error (RMSE) of the robot tip (and body) pose, which we compute as

$$d_{\text{RMSE, pos}} = \frac{1}{L} \sqrt{\frac{1}{N} \sum_{n=1}^N \|\tilde{\mathbf{p}}_n - \mathbf{p}_n\|_2^2}, \quad (50a)$$

$$d_{\text{RMSE, rot}} = \sqrt{\frac{1}{N} \sum_{n=1}^N \|\ln(\tilde{\mathbf{R}}_n \mathbf{R}_n^{-1})^\vee\|_2^2}. \quad (50b)$$

IV. RESULTS

A. (Simulation) Robot Extension

The estimator is evaluated on the extensible robot simulation trajectory ‘Extensible’. The trajectory is a simple extension and contraction of the robot, with no external forces applied. The estimator is able to produce a estimate of the robot’s state, with an average tip error of 0.195% and an average body error of 0.400%. A side-by-side comparison of the simulated robot and the estimate result is shown in Fig. 6. The estimator on this trajectory has an average NEES of 7.605, indicating that the covariance estimate is slightly overconfident. The estimator demonstrates a smoothing effect in time when the robot engages in sudden changes in velocity. A clear example of this is when the estimator does not fully contract to zero length as the simulator does, behaviour clearly visible in the first column of Fig. 6. During this sudden acceleration, the estimator GP smooths the estimate, resulting in a brief

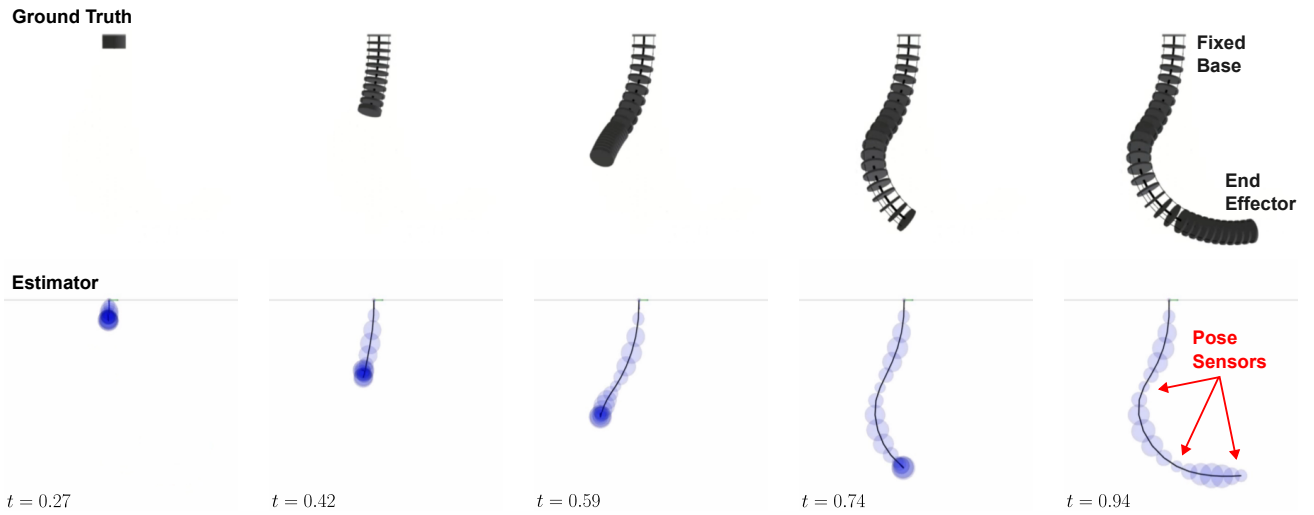


Fig. 6. Comparison of the estimator (bottom) and the simulation (top) showing an extensible robot during the ‘Extensible’ trajectory using four pose sensors at five different timesteps. The estimator demonstrates its ability to generalize to an extensible robot configuration here, highlighting the method’s versatility across multiple robot types. The demo shown has an average tip error of 0.195%. Time nodes are placed at a rate of 30Hz with no interpolated states added after the fact.

period of overconfidence. Similar smoothing behaviour is seen spatially in the works [36] and [40].

B. Comparison to 1D GP Prior

To compare the two approaches, both are evaluated on the ‘Out-of-Bounds’ trajectory. The quasi-static method is applied to each timestep containing a measurement at $K = 462$ with $N = 17$ spatial nodes. Fig. 7 contains the results of both methods. As expected, the quasi-static method is able to produce reasonable estimates, but is sensitive to high-frequency noise in the sensor data over time. This is clear when zooming in on the time series data for the tip position, where visible jitter is present. In contrast, the proposed method is able to smooth out the estimate in time. Another region of interest is when no data is available. In ‘Out-of-Bounds’ this occurs when the robot tip leaves the Aurora workspace. During this time, the quasi-static method does not have a well-defined behaviour. The proposed method, however, is able to generate a reasonable estimate while accounting for the increased uncertainty in its confidence bounds.

More interestingly, the proposed method also produces a more confident estimate even when data is available. This comes from the fact that it can leverage information at other points in time to refine its estimate. This is particularly evident in the case shown, which is solved using batch estimation, but a similar effect is expected in a sliding window implementation, albeit while lacking information about future data points. Accuracy cannot be directly compared between these two methods as the quasi-static method does not have interpolation capability in time, and so evaluation at the asynchronous ground truth time steps is not possible.

C. Dynamic Trajectories

The estimator is evaluated on five different dynamic trajectories, each with varying levels of external contact and operated at different speeds. Table I contains the performance

metrics for each trajectory in addition to a description of each trajectory. In ‘Fast Contact’, large external forces are applied to the robot at two points in the trajectory. A side-by-side comparison of the estimator and the real robot is shown in Fig. 8. The estimator is able to maintain a reasonable estimate of the robot’s state despite the unmodelled external forces. The average tip error for this trajectory is 1.162%, and the average body error is 3.851%. The estimator has an average NEES of 4.355, indicating that the covariance estimate is slightly underconfident. A closer look at the tip position estimate compared to the ground truth is shown in Fig. 9. We note that in the regions where strong external forces are applied, the estimator may experience overconfidence in its estimate. This is a result of the GP smoothing effect, which can cause the estimate to be less responsive to sudden changes in the robot’s strains or velocities. When external forces are not applied, the estimator’s confidence bounds quickly return to being consistent with the ground truth. Given that no explicit contact model is used, with external forces only being implicitly accounted for in the sensor data, this result is promising and points to this method only improving with additional sensor data (e.g., strain sensing).

Throughout each of the trajectories, the estimator is able to produce reasonable estimates of the robot’s state. Average tip errors remain below 2% for all trajectories when pose measurements are used. This is on the order of the noise from the pose sensors used. For each trajectory, we also see that the tip estimate is either improved or remains similar with the addition of gyroscope measurements into the system. This result is most prevalent in the ‘Out-of-Bounds’ trajectory, where the pose measurements are not available for portions of the trajectory. In this dropout scenario, the use of both sources of measurements greatly improves the estimate, highlighting the benefit of using multiple sensor modalities.

A brief runtime analysis is shown in Fig. 10 for the ‘Fast Contact’ trajectory, estimating only the mean of the state. The implementation scales linearly with respect to the number of

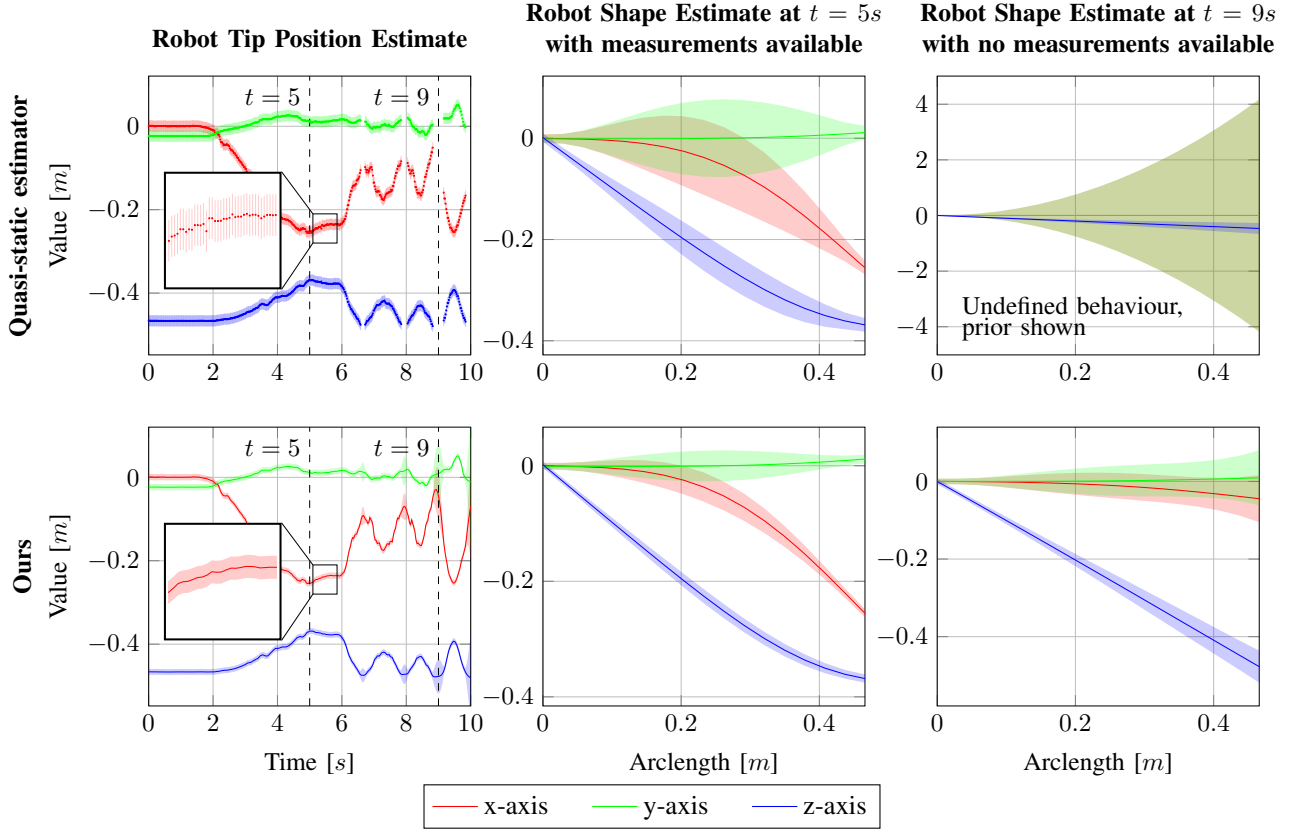


Fig. 7. Comparison to the quasi-static benchmark on the ‘Out-of-Bounds’ trajectory using end effector pose measurements. The leftmost column shows the robot tip position over time for both the proposed method and the quasi-static estimator. The right two columns show a comparison between the two methods at two different time steps, $t = 5s$ and $t = 9s$. When data at a particular timestep is available (e.g., middle column), the two methods produce similar mean estimates, with our new method having higher amounts of certainty despite using the same noise characteristics in the arclength WNOA model. The additional information provided in time allows the proposed method to produce a more confident estimate, making it less sensitive to high-frequency noise. When data is not available (e.g., right column), the quasi-static benchmark does not have well-defined behaviour and is unable to produce a reasonable estimate.

TABLE I
PERFORMANCE METRICS AND TRAJECTORY DESCRIPTION FOR BOTH SIMULATED AND EXPERIMENTAL TRAJECTORIES.

Trial	MAE (Tip)		MAE (Body)		RMSE (Tip)		RMSE (Body)		Average NEES	Trajectory description
	Pos (%)	Rot (rad)	Pos (%)	Rot (rad)	Pos (%)	Rot (rad)	Pos (%)	Rot (rad)		
Extensible										
Pose only	0.195	0.014	0.400	0.014	0.225	0.021	0.286	0.020	7.605	Simulated TDCR moving steadily from a curved fully extended position, all the way contracted, and back out.
Gyro only	-	-	-	-	-	-	-	-	-	
Fused	-	-	-	-	-	-	-	-	-	
Out-of-Bounds										
Pose only	1.546	0.044	5.225	0.113	2.205	0.063	2.896	0.139	8.463	A dynamic trajectory powered by tendon actuation. Some pose data is lost as the robot leaves the sensor workspace.
Gyro only	15.240	0.668	13.589	0.337	15.848	0.709	10.931	0.422	9.009	
Fused	1.447	0.038	5.211	0.108	1.843	0.041	2.829	0.132	9.028	
Fast Contact										
Pose only	1.163	0.035	3.847	0.076	1.275	0.037	2.052	0.088	4.208	A dynamic trajectory achieved through applying sustained external contacts. Fast oscillations present.
Gyro only	14.238	0.251	12.625	0.191	17.445	0.269	11.151	0.221	2.910	
Fused	1.162	0.036	3.851	0.071	1.274	0.038	2.054	0.083	4.355	
Impulse 1										
Pose only	1.558	0.039	4.880	0.103	1.690	0.042	2.742	0.120	7.361	The robot responds to multiple applied impulse contacts. Fast oscillations present.
Gyro only	20.646	0.259	17.307	0.278	21.353	0.263	14.209	0.298	3.737	
Fused	1.557	0.039	4.866	0.099	1.690	0.042	2.730	0.114	7.712	
Impulse 2										
Pose only	1.307	0.044	4.370	0.100	1.398	0.049	2.306	0.118	5.712	The robot responds to multiple applied impulse contacts.
Gyro only	19.438	0.314	17.157	0.247	21.869	0.324	14.709	0.275	4.601	
Fused	1.305	0.045	4.365	0.091	1.395	0.051	2.302	0.108	5.896	
Slow Free Space										
Pose only	1.099	0.042	4.073	0.092	1.161	0.042	2.204	0.116	6.860	A slow trajectory actuated via tendon actuation without any external contact applied.
Gyro only	14.542	0.840	9.461	0.325	14.892	0.874	8.493	0.461	5.680	
Fused	1.098	0.042	4.071	0.092	1.160	0.042	2.202	0.116	7.132	

The best performing sensor configuration for each metric on each trial is bolded. For both the MAE and RMSE errors, this is the lowest value. For the NEES metric, this is the value closest to 6, the number of DoFs in the pose states being evaluated.

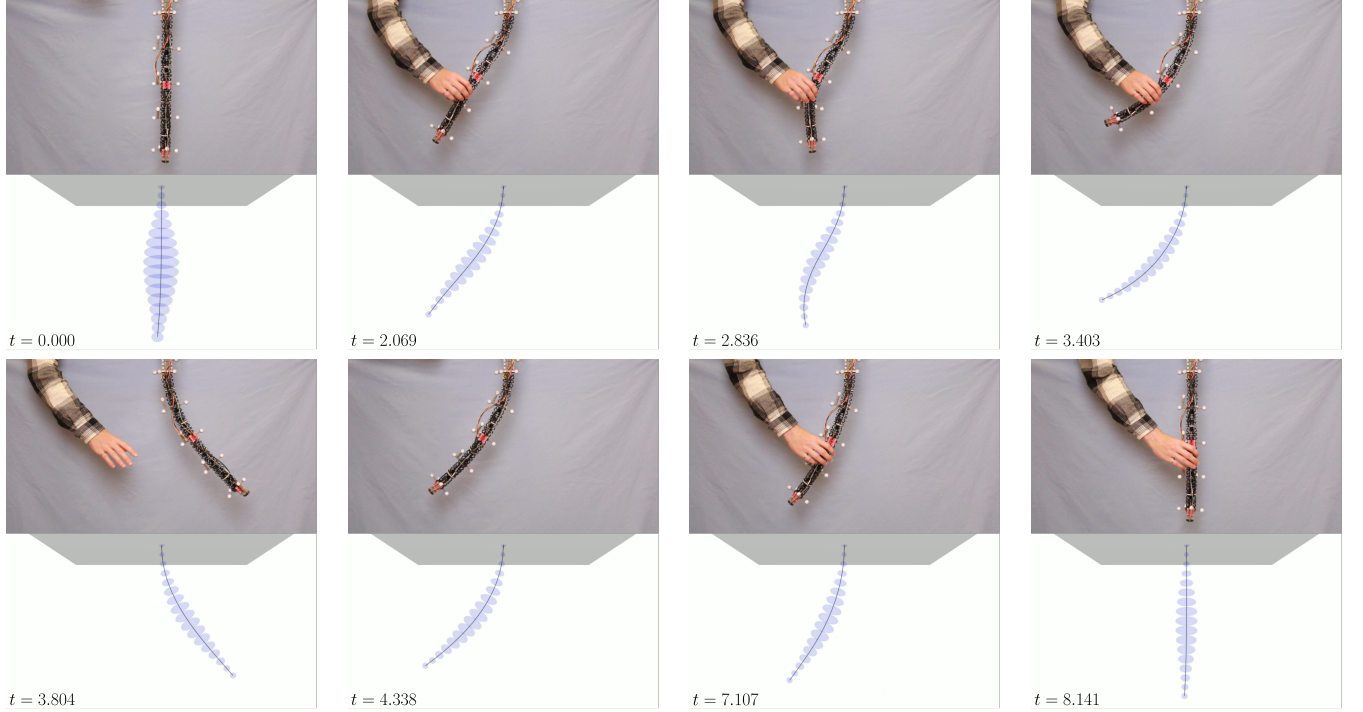


Fig. 8. Comparison of the estimator (bottom) and a video (top) recording of the robot during the ‘Fast Contact’ trajectory using both pose and gyroscope sensors at eight different timesteps. The estimator demonstrates its ability to maintain reasonable estimates of the robot’s state when unmodelled external forces are applied. The demo shown has an average tip error of 1.162%. Time nodes are placed at a rate of 30Hz with no interpolated states added after the fact.

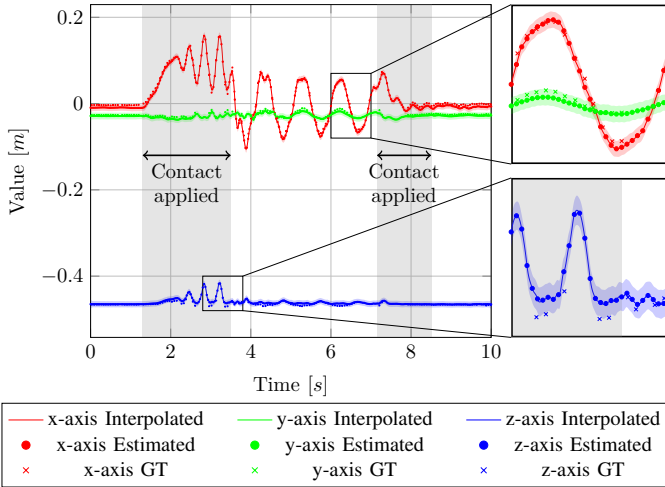


Fig. 9. Robot tip position estimate during the ‘Fast Contact’ fused data trajectory. In this demo, external forces are applied to the robot and noted by the shaded regions. Ground truth values are shown as points, while the estimated mean and 3- σ bounds are shown as solid lines and shaded regions, respectively. Interpolation in time is performed after the fact, showing 10 interpolated nodes between each estimated one. The estimator is able to maintain a reasonable estimate of the robot’s state despite the unmodelled external forces. We note that during aggressive external forces (bottom zoomed region), the estimator may experience overconfidence in its estimate.

time nodes K , a result predicted from the sparsity of the problem. Similarly, cubic scaling is observed with respect to the number of spatial nodes N , as predicted.

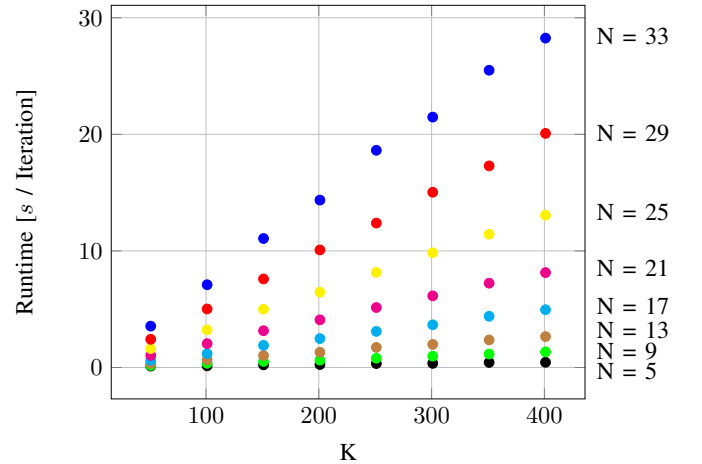


Fig. 10. Runtime comparison for the ‘Fast Contact’ fused data estimate. The runtime shown is for estimating only the mean of the state. The proposed implementation runtime scales linearly with respect to the number of time nodes K , a result predicted from the sparsity of the problem. Cubic scaling is also observed with respect to the number of spatial nodes N , as predicted.

D. Interpolation Validation

While interpolation in time is performed constantly during the solve in order to include asynchronous measurements, the states are not explicitly stored. After the solve, however, we can interpolate in time and space (though not simultaneously). Fig. 9 shows the time-interpolated tip position estimate during the ‘Fast Contact’ trajectory. Each estimated node contains 10 interpolated nodes in between, resulting in the display of 300 nodes / second. Because of the ‘white-noise-on-acceleration’

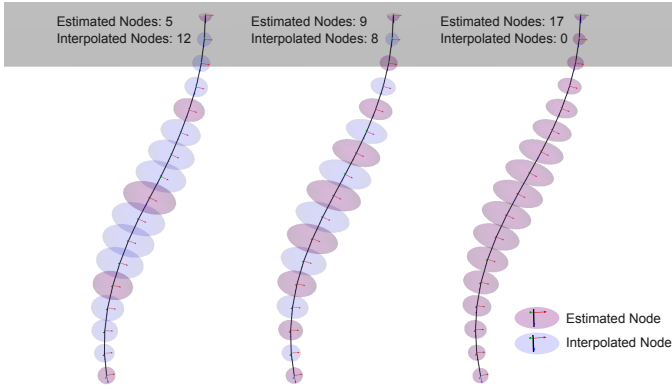


Fig. 11. A snapshot of the ‘Fast Contact’ fused data estimate at time $t = 2.833$ (the third panel in Fig. 8) with three different selections of N . For each of the $N = 5, 9, 17$ cases, interpolation is performed so that 17 total nodes are displayed. As N increases, the covariance estimates slightly decreases. The change also results in small deviations in the mean estimate.

assumption in the models from Section II-C, the interpolated states form a series of cubic splines in the associated Lie algebra, which remain smooth in time.

Similarly, Fig. 11 shows interpolation in space for the same trajectory at a single time step. A similar cubic spline behaviour is observed with the interpolated states. When solving the same problem with different numbers of spatial nodes N , we see that the covariance estimate decreases slightly as N increases, and the mean estimate changes slightly. Some change is expected as with more spatial nodes, the Euler step approximation used in the creation of the prior factors takes a smaller step, resulting in a more finely discretized system. We can quantify this effect to get an approximation for the order of variation introduced by a choice of discretization by treating one estimate using fully estimated nodes as a ‘ground truth’ and comparing solves that replace estimated nodes with interpolated ones. For the cases in Figure 11, we do just this and find that the $N = 5$ case has an average ‘tip error’ of 0.11% and a ‘body error’ of 0.38% while the $N = 9$ case has an average ‘tip error’ of 0.06% and a ‘body error’ of 0.21%. While this result does not provide insight into the accuracy effects of the choice of N , it does indicate that the larger the discretization step used, the more deviation from a more finely discretized solution we can expect. Users of the method should keep this in mind when selecting a value of N for their application.

V. DISCUSSION

This work introduces continuous-time stochastic estimation to the domain of continuum robots. By providing an uncertainty-aware estimate, one can better make decisions surrounding required sensor placements and collection rates given a specified task. While we chose to use a configuration tuned towards as close to an NEES value of six across all experiments as possible, this came at the expense of being overconfident in some higher contact scenarios. Users of this framework may wish to err on the side of overconfidence if such high-impact scenarios are expected in their application.

We qualitatively confirm the theoretical runtime properties of the proposed estimator, demonstrating linear scaling with respect to the number of time nodes and cubic scaling with respect to the number of spatial nodes. Also demonstrated is competitive accuracy ($< 2\%$ tip error) with approximately ‘real-time’ solve rates (30Hz) when only the mean is computed. This result is demonstrated across a variety of robot motions, external contacts, and two different robot types (extensible and non-extensible). We demonstrate the inclusion of multiple asynchronous sensor modalities and open the possibility for the addition of any number of other sensors, highlighting the flexibility of the framework.

The approximations made in this work follow similar assumptions to those made in previous continuous estimation works [36], [37]. These include the approximate linearizations of relevant Jacobians and the independence assumption between the interpolated states used in the measurement models. The latter of these assumptions does have a notable impact on the state estimate, a fact that becomes prohibitively worse with lower estimation node rates. In practice, we find that approximate ‘real-time’ solve rates can be achieved with estimation node rates of 30Hz, provided only the mean is computed. It is left to future work to explore computationally efficient methods for computing the covariance in real-time. Apart from the motivating works, we make further assumptions surrounding the dynamic Cosserat rod model via the WNOA Cosserat rod dynamics. This choice surely limits the accuracy of the estimator compared to the more sophisticated models of [18], [44], a trade-off that may be worth it given the flexibility of the estimator when handling asynchronous input data streams and its additional covariance estimation capacity.

VI. CONCLUSION

In this work, we presented a fully stochastic, continuous-time estimation framework for continuum robots by extending the works of [36] and [37] to the domain of continuum robot trajectory estimation (i.e., space and time). We demonstrated the ability of the framework to fuse asynchronous measurements from multiple sensor modalities in an uncertainty-aware way. Alongside this work, we provide an open-source implementation of our method to the research community at <https://github.com>.

By formulating the continuous-time trajectory estimation of a continuum robot as a factor-graph optimization problem, we hope to open the door to further cross-domain adaptation from works established in mobile robotics. This framework provides a flexible foundation for the addition of other sensors such as cameras, IMUs, or strain gauges, as well as the incorporation of more complex factor graph-based algorithms used for localization, mapping, and sliding window filtering. To the best of our knowledge, this is the first stochastic continuous-time state estimation framework for continuum robots, and we hope it will serve as a useful tool for the community to build upon.

APPENDIX A NOTATION

Throughout this work we use the notation of [43]. Mean values are represented with a bar, \bar{x} . Posterior values are

represented with a hat, \hat{x} . Lastly, prior values are represented with a check, \check{x} . Lower case, non-bolded (e.g. x) characters represent scalars, vectors are lower case, bolded (e.g. \mathbf{x}), and matrices are upper case, bolded (e.g. \mathbf{X}).

We define the hat and curly hat operator for the three and six dimensional vectors, $\mathbf{x}, \boldsymbol{\rho}, \boldsymbol{\phi} \in \mathbb{R}^3, \boldsymbol{\xi} = \begin{bmatrix} \boldsymbol{\rho} \\ \boldsymbol{\phi} \end{bmatrix} \in \mathbb{R}^6$, as

$$\mathbf{x}^\wedge = \begin{bmatrix} 0 & -x_3 & x_2 \\ x_3 & 0 & -x_1 \\ -x_2 & x_1 & 0 \end{bmatrix}, \quad (51)$$

$$\boldsymbol{\xi}^\wedge = \begin{bmatrix} \boldsymbol{\phi}^\wedge & \boldsymbol{\rho} \\ \mathbf{0}^T & 0 \end{bmatrix}, \quad (52)$$

$$\boldsymbol{\xi}^\lambda = \begin{bmatrix} \boldsymbol{\phi}^\wedge & \boldsymbol{\rho}^\wedge \\ \mathbf{0} & \boldsymbol{\phi}^\wedge \end{bmatrix}. \quad (53)$$

The inverse of the wedge operator is defined as

$$(\mathbf{X}^\vee)^\wedge = \mathbf{X}, \quad (\mathbf{x}^\wedge)^\vee = \mathbf{x}. \quad (54)$$

All transformations are represented as $\mathbf{T}_{bi} \in SE(3)$, denoting the inertial frame pose relative to the body frame. A natural consequence of this notation that differs from many works in the continuum robotics literature is that the Jacobian \mathcal{J} is the left Jacobian of $SE(3)$ and that body-frame kinematics are applied to the left side of a transformation. For example, the kinematic equation for a pose with some body-centric velocity $\boldsymbol{\omega}_b(t) \in \mathbb{R}^6$ is given by

$$\frac{\partial \mathbf{T}_{bi}(t)}{\partial t} = \boldsymbol{\omega}_b(t)^\wedge \mathbf{T}_{bi}(t). \quad (55)$$

In general, we will not explicitly include the bi and b subscripts. A superscript containing a number inside of parentheses, (e.g., $\mathbf{x}^{(i)}$) denotes the i th index of that object and will be used when conflicting super/subscripts are present.

APPENDIX B JACOBIANS

Time Factor

The time error terms are linearized as

$$\mathbf{e}_{\text{time}}^{(n,k)} \approx \bar{\mathbf{e}}_{\text{time}}^{(n,k)} + \begin{bmatrix} \mathbf{F}_{\text{time}}^{(n,k)} & \mathbf{E}_{\text{time}}^{(n,k)} \end{bmatrix} \begin{bmatrix} \delta \mathbf{x}_{n,k} \\ \delta \mathbf{x}_{n,k+1} \end{bmatrix}, \quad (56)$$

$$\mathbf{F}_{\text{time}}^{(n,k)} = \begin{bmatrix} -\mathcal{J}_{n,k}^{(t)-1} \mathcal{T}_{n,k}^{(t)} & \mathbf{0} & -\Delta t \mathbf{I} \\ \mathbf{0} & -\mathbf{I} & \mathbf{0} \\ \mathbf{0} & \mathbf{0} & -\mathbf{I} \end{bmatrix}, \quad (57)$$

$$\mathbf{E}_{\text{time}}^{(n,k)} = \begin{bmatrix} \mathcal{J}_{n,k}^{(t)-1} & \mathbf{0} & \mathbf{0} \\ \mathbf{0} & \mathbf{I} & \mathbf{0} \\ \mathbf{0} & \mathbf{0} & \mathbf{I} \end{bmatrix}, \quad (58)$$

$$\mathcal{J}_{n,k}^{(t)} = \mathcal{J}(\ln(\mathbf{T}_{n,k+1} \mathbf{T}_{n,k}^{-1})^\vee), \quad (59)$$

$$\mathcal{T}_{n,k}^{(t)} = \text{Ad}(\mathbf{T}_{n,k+1} \mathbf{T}_{n,k}^{-1}). \quad (60)$$

Space Factor

The space error terms are linearized as

$$\mathbf{e}_{\text{space}}^{(n,k)} \approx \bar{\mathbf{e}}_{\text{space}}^{(n,k)} + \begin{bmatrix} \mathbf{F}_{\text{space}}^{(n,k)} & \mathbf{E}_{\text{space}}^{(n,k)} \end{bmatrix} \begin{bmatrix} \delta \mathbf{x}_{n,k} \\ \delta \mathbf{x}_{n+1,k} \end{bmatrix}, \quad (61)$$

$$\mathbf{F}_{\text{space}}^{(n,k)} = \begin{bmatrix} -\mathcal{J}_{n,k}^{(s)-1} \mathcal{T}_{n,k}^{(s)} & -\Delta s \mathbf{I} & \mathbf{0} \\ \mathbf{0} & -\mathbf{I} & \mathbf{0} \\ \mathbf{0} & \Delta s \boldsymbol{\omega}_{n,k}^\lambda & -\mathbf{I} - \Delta s \boldsymbol{\epsilon}_{n,k}^\lambda \end{bmatrix}, \quad (62)$$

$$\mathbf{E}_{\text{space}}^{(n,k)} = \begin{bmatrix} \mathcal{J}_{n,k}^{(s)-1} & \mathbf{0} & \mathbf{0} \\ \mathbf{0} & \mathbf{I} & \mathbf{0} \\ \mathbf{0} & \mathbf{0} & \mathbf{I} \end{bmatrix}, \quad (63)$$

$$\mathcal{J}_{n,k}^{(s)} = \mathcal{J}(\ln(\mathbf{T}_{n+1,k} \mathbf{T}_{n,k}^{-1})^\vee), \quad (64)$$

$$\mathcal{T}_{n,k}^{(s)} = \text{Ad}(\mathbf{T}_{n+1,k} \mathbf{T}_{n,k}^{-1}). \quad (65)$$

Unary Factor

The unary error terms are linearized as

$$\mathbf{e}_{\text{boundary}}^{(n,k)} \approx \bar{\mathbf{e}}_{\text{boundary}}^{(n,k)} + \mathbf{E}_{\text{boundary}}^{(n,k)} \delta \mathbf{x}_{n,k}, \quad (66)$$

$$\mathbf{E}_{\text{boundary}}^{(n,k)} = \begin{bmatrix} -\mathcal{J}_{n,k}^{-1} \mathcal{T}_{n,k} & \mathbf{0} & \mathbf{0} \\ \mathbf{0} & -\mathbf{I} & \mathbf{0} \\ \mathbf{0} & \mathbf{0} & -\mathbf{I} \end{bmatrix}, \quad (67)$$

$$\mathcal{J}_{n,k} = \mathcal{J}(\ln(\mathbf{T}_0^{(n,k)} \mathbf{T}_{n,k}^{-1})^\vee), \quad (68)$$

$$\mathcal{T}_{n,k} = \text{Ad}(\mathbf{T}_0^{(n,k)} \mathbf{T}_{n,k}^{-1}). \quad (69)$$

Pose Measurement Factor

The pose measurement error terms are linearized as

$$\mathbf{e}_{\text{pose}} \approx \bar{\mathbf{e}}_{\text{pose}} + \mathbf{E}_{\text{pose}} \delta \mathbf{x}_{n,k} \quad (70)$$

$$\mathbf{E}_{\text{pose}} = [-\tilde{\mathcal{J}}_{n,k} \tilde{\mathcal{T}}_{n,k} \quad \mathbf{0} \quad \mathbf{0}], \quad (71)$$

$$\tilde{\mathcal{J}}_{n,k} = \mathcal{J}(\ln(\tilde{\mathbf{T}}_{n,k} \mathbf{T}_{n,k}^{-1})^\vee), \quad (72)$$

$$\tilde{\mathcal{T}}_{n,k} = \text{Ad}(\tilde{\mathbf{T}}_{n,k} \mathbf{T}_{n,k}^{-1}). \quad (73)$$

Gyro Measurement Factor

The gyro measurement error terms are linearized as

$$\mathbf{e}_{\text{gyro}} \approx \bar{\mathbf{e}}_{\text{gyro}} + \mathbf{E}_{\text{gyro}} \delta \mathbf{x}_{n,k}, \quad (74)$$

$$\mathbf{E}_{\text{gyro}} = \begin{bmatrix} \mathbf{0} & \mathbf{0} & \begin{bmatrix} \mathbf{0} & \mathbf{0} \\ \mathbf{0} & \mathbf{I} \end{bmatrix} \end{bmatrix}. \quad (75)$$

Interpolation Jacobians

The following Jacobians are the approximate linearized Jacobians for the time-interpolation. Spatial interpolation Jacobians will take a similar form. We wish to represent a perturbation to an interpolated state with respect to a perturbation of the estimation states. That is,

$$\delta \mathbf{x}(s, t) \approx \frac{\partial \mathbf{x}(s, t)}{\partial \mathbf{x}_{n,k}^\square} \delta \mathbf{x}_{n,k}^\square, \quad (76)$$

$$\mathbf{x}_{n,k}^\square = \begin{bmatrix} \mathbf{x}_{n,k} \\ \mathbf{x}_{n,k+1} \end{bmatrix}. \quad (77)$$

The Jacobians are

$$\delta t_{s,t} \approx \underbrace{\left(\mathcal{J}_{s,t} P_1 \Lambda_{s,t} \frac{\partial \gamma_{n,k}^\square}{\partial x_{n,k}^\square} + \mathcal{T}_{s,t} P_1^* \right)}_{\frac{\partial t_{s,t}}{\partial x_{n,k}^\square}} \delta x_{n,k}^\square, \quad (78)$$

$$\delta \epsilon_{s,t} \approx \underbrace{\left(\mathcal{J}_{s,t} P_2 - \frac{1}{2} (P_2 \Lambda_{s,t} \bar{\gamma}_{n,k}^\square)^\wedge P_1 \right) \Lambda_{s,t} \frac{\partial \gamma_{n,k}^\square}{\partial x_{n,k}^\square}}_{\frac{\partial \epsilon_{s,t}}{\partial x_{n,k}^\square}} \delta x_{n,k}^\square, \quad (79)$$

$$\delta \varpi_{s,t} \approx \underbrace{\left(\mathcal{J}_{s,t} P_3 - \frac{1}{2} (P_3 \Lambda_{s,t} \bar{\gamma}_{n,k}^\square)^\wedge P_1 \right) \Lambda_{s,t} \frac{\partial \gamma_{n,k}^\square}{\partial x_{n,k}^\square}}_{\frac{\partial \varpi_{s,t}}{\partial x_{n,k}^\square}} \delta x_{n,k}^\square, \quad (80)$$

where P_i is a selection matrix for the i th block. Specifically, it's a 3×1 block matrix where the i th column is identity, and each block is 6×6 . P_1^* selects the first block of a block vector with 6 blocks of size 6. Furthermore,

$$\mathcal{J}_{s,t} = \mathcal{J}(\ln(T(s,t)T_{n,k}^{-1})^\vee), \quad (81)$$

$$\mathcal{T}_{s,t} = \text{Ad}(T(s,t)T_{n,k}^{-1}), \quad (82)$$

$$\frac{\partial \gamma_{n,k}^\square}{\partial x_{n,k}^\square} = \begin{bmatrix} J_1 & \mathbf{0} \\ J_2 & J_3 \end{bmatrix}, \quad (83)$$

$$J_1 = \begin{bmatrix} \mathbf{0} & & \\ & I & \\ & & I \end{bmatrix}, \quad (84)$$

$$J_2 = \begin{bmatrix} -\mathcal{J}_{s,t}^{-1} \mathcal{T}_{s,t} & \mathbf{0} & \mathbf{0} \\ -\frac{1}{2} \epsilon_{s,t}^\wedge \mathcal{J}_{s,t}^{-1} \mathcal{T}_{s,t} & \mathbf{0} & \mathbf{0} \\ -\frac{1}{2} \varpi_{s,t}^\wedge \mathcal{J}_{s,t}^{-1} \mathcal{T}_{s,t} & \mathbf{0} & \mathbf{0} \end{bmatrix}, \quad (85)$$

$$J_3 = \begin{bmatrix} \mathcal{J}_{s,t}^{-1} & \mathbf{0} & \mathbf{0} \\ \frac{1}{2} \epsilon_{s,t}^\wedge \mathcal{J}_{s,t}^{-1} & \mathcal{J}_{s,t}^{-1} & \mathbf{0} \\ \frac{1}{2} \varpi_{s,t}^\wedge \mathcal{J}_{s,t}^{-1} & \mathbf{0} & \mathcal{J}_{s,t}^{-1} \end{bmatrix}. \quad (86)$$

APPENDIX C PARAMETERS

Simulation Parameters

The parameters used in the simulation experiment are

$$R_{\text{pose}} = \text{diag}\{1 \times 10^{-5}, 1 \times 10^{-5}, 1 \times 10^{-5}, 2.5 \times 10^{-4}, 2.5 \times 10^{-4}, 2.5 \times 10^{-4}\}, \quad (87a)$$

$$Q_0 = \text{diag}\{4.0 \times 10^{-7}, 4.0 \times 10^{-7}, 4.0 \times 10^{-7}, 5.0 \times 10^{-4}, 5.0 \times 10^{-4}, 5.0 \times 10^{-4}, 5.0 \times 10^{-3}, 5.0 \times 10^{-3}, 5.0 \times 10^6, 5.0 \times 10^2, 5.0 \times 10^2, 5.0 \times 10^{-5}, 5.0 \times 10^1, 5.0 \times 10^1, 5.0 \times 10^1, 5.0 \times 10^1, 5.0 \times 10^1\} \quad (87b)$$

$$Q_1 = \text{diag}\{1.5 \times 10^0, 1.5 \times 10^0, 1.5 \times 10^0, 2.5 \times 10^1, 2.5 \times 10^1, 2.5 \times 10^1\} \quad (87c)$$

$$Q_2 = \text{diag}\{4.0 \times 10^{-2}, 4.0 \times 10^{-2}, 4.0 \times 10^{-2},$$

$$5 \times 10^2, 5 \times 10^2, 5 \times 10^2\} \quad (87d)$$

$$Q_3 = \text{diag}\{1.5 \times 10^1, 1.5 \times 10^1, 1.5 \times 10^1, 1.5 \times 10^1, 1.5 \times 10^1, 1.5 \times 10^1\}. \quad (87e)$$

Experiment Parameters

The parameters used in the real-world experiments are

$$R_{\text{pose}} = \text{diag}\{2 \times 10^{-5}, 2 \times 10^{-5}, 2 \times 10^{-5}, 2.5 \times 10^{-3}, 2.5 \times 10^{-3}, 2.5 \times 10^{-3}\}, \quad (88a)$$

$$R_{\text{gyro}} = \text{diag}\{1 \times 10^{-6}, 1 \times 10^{-6}, 1 \times 10^{-6}\}, \quad (88b)$$

$$Q_0 = \text{diag}\{1.2 \times 10^{-5}, 1.2 \times 10^{-5}, 1.2 \times 10^{-5}, 1.5 \times 10^{-4}, 1.5 \times 10^{-4}, 1.5 \times 10^{-4}, 1.5 \times 10^{-3}, 1.5 \times 10^{-3}, 1.5 \times 10^{-3}, 1.5 \times 10^2, 1.5 \times 10^2, 1.5 \times 10^{-5}, 1.5 \times 10^1, 1.5 \times 10^1, 1.5 \times 10^1, 1.5 \times 10^1, 1.5 \times 10^1, 1.5 \times 10^1\} \quad (88c)$$

$$Q_1 = \text{diag}\{1.5 \times 10^0, 1.5 \times 10^0, 1.5 \times 10^0, 1.2 \times 10^3, 1.2 \times 10^3, 1.2 \times 10^3\} \quad (88d)$$

$$Q_2 = \text{diag}\{1.2 \times 10^{-1}, 1.2 \times 10^{-1}, 1.2 \times 10^{-1}, 1.5 \times 10^2, 1.5 \times 10^2, 1.5 \times 10^2\} \quad (88e)$$

$$Q_3 = \text{diag}\{1.2 \times 10^{-1}, 1.2 \times 10^{-1}, 1.2 \times 10^{-1}, 1.5 \times 10^3, 1.5 \times 10^3, 1.5 \times 10^3\}. \quad (88f)$$

REFERENCES

- [1] G. Robinson and J. B. Davies, "Continuum robots - a state of the art," *Proceedings - IEEE International Conference on Robotics and Automation*, vol. 4, 1999.
- [2] J. Burgner-Kahrs, D. C. Rucker, and H. Choset, "Continuum robots for medical applications: A survey," *IEEE Transactions on Robotics*, vol. 31, no. 6, pp. 1261–1280, 2015.
- [3] P. E. Dupont, N. Simaan, H. Choset, and C. Rucker, "Continuum robots for medical interventions," *Proceedings of the IEEE*, vol. 110, no. 7, pp. 847–870, 2022.
- [4] X. Dong, D. Axinte, D. Palmer, S. Cobos, M. Raffles, A. Rabani, and J. Kell, "Development of a slender continuum robotic system for on-wing inspection/repair of gas turbine engines," *Robotics and Computer-Integrated Manufacturing*, vol. 44, 2017.
- [5] M. Wang, X. Dong, W. Ba, A. Mohammad, D. Axinte, and A. Norton, "Design, modelling and validation of a novel extra slender continuum robot for in-situ inspection and repair in aeroengine," *Robotics and Computer-Integrated Manufacturing*, vol. 67, p. 102054, 2021.
- [6] E. W. Hawkes, L. H. Blumenschein, J. D. Greer, and A. M. Okamura, "A soft robot that navigates its environment through growth," *Science Robotics*, vol. 2, no. 8, p. eaan3028, 2017.
- [7] C. Armanini, F. Boyer, A. T. Mathew, C. Duriez, and F. Renda, "Soft robots modeling: A structured overview," *IEEE Transactions on Robotics*, vol. 39, no. 3, pp. 1728–1748, 2023.
- [8] C. Della Santina, C. Duriez, and D. Rus, "Model-based control of soft robots: A survey of the state of the art and open challenges," *IEEE Control Systems Magazine*, vol. 43, no. 3, pp. 30–65, 2023.
- [9] R. J. Roesthuis, M. Kemp, J. J. van den Dobbelsteen, and S. Misra, "Three-dimensional needle shape reconstruction using an array of fiber bragg grating sensors," *IEEE/ASME Transactions on Mechatronics*, vol. 19, no. 4, pp. 1115–1126, 2014.
- [10] S. Song, Z. Li, H. Yu, and H. Ren, "Electromagnetic positioning for tip tracking and shape sensing of flexible robots," *IEEE Sensors Journal*, vol. 15, no. 8, pp. 4565–4575, 2015.
- [11] B. Kim, J. Ha, F. C. Park, and P. E. Dupont, "Optimizing curvature sensor placement for fast, accurate shape sensing of continuum robots," in *2014 IEEE International Conference on Robotics and Automation (ICRA)*, 2014, pp. 5374–5379.

- [12] G. Pei and J. Hughes, "Polynomial curvature model for imu-based proprioception in soft robotic manipulators under external forces," in *IEEE 8th International Conference on Soft Robotics*, 2025, pp. 1–7.
- [13] L. Liu, X. Huang, X. Zhang, B. Zhang, H. Xu, V. M. Trivedi, K. Liu, Z. Shaikh, and H. Zhao, "Model-based 3d shape reconstruction of soft robots via distributed strain sensing," *Soft Robotics*, 2025.
- [14] F. Stella, C. Della Santina, and J. Hughes, "Soft robot shape estimation with imus leveraging pcc kinematics for drift filtering," *IEEE Robotics and Automation Letters*, vol. 9, no. 2, pp. 1945–1952, 2023.
- [15] H. Abdelaziz, A. Nada, H. Ishii, and H. El-Hussieny, "State estimation of continuum robots: A nonlinear constrained moving horizon approach," 2023, *arXiv:2308.03931*.
- [16] W. S. Rone and P. Ben-Tzvi, "Multi-segment continuum robot shape estimation using passive cable displacement," in *2013 IEEE International Symposium on Robotic and Sensors Environments (ROSE)*, 2013, pp. 37–42.
- [17] V. K. Venkiteswaran, J. Sikorski, and S. Misra, "Shape and contact force estimation of continuum manipulators using pseudo rigid body models," *Mechanism and Machine Theory*, vol. 139, pp. 34–45, 2019.
- [18] T. Zheng, Q. Han, and H. Lin, "Full state estimation of continuum robots from tip velocities: A cosserat-theoretic boundary observer," *IEEE Transactions on Automatic Control*, vol. 70, no. 5, pp. 2859–2872, 2025.
- [19] T. Zheng, C. McFarland, M. Coad, and H. Lin, "Estimating infinite-dimensional continuum robot states from the tip," in *IEEE 7th International Conference on Soft Robotics*. IEEE, 2024, pp. 572–578.
- [20] T. Zheng and J. Burgner-Kahrs, "Estimating dynamic soft continuum robot states from boundaries," 2025, *arXiv:2505.04491*.
- [21] D. Feliu-Talegon, A. T. Mathew, A. Y. Alkayes, Y. A. Adamu, and F. Renda, "Dynamic shape estimation of tendon-driven soft manipulators via actuation readings," *IEEE Robotics and Automation Letters*, vol. 10, no. 1, pp. 780–787, 2025.
- [22] Q. Zhao, J. Lai, K. Huang, X. Hu, and H. K. Chu, "Shape estimation and control of a soft continuum robot under external payloads," *IEEE/ASME Transactions on Mechatronics*, vol. 27, no. 5, pp. 2511–2522, 2021.
- [23] G. Zhan, X. An, Y. Jiang, J. Duan, H. Zhao, and S. E. Li, "Physics informed neural pose estimation for real-time shape reconstruction of soft continuum robots," *IEEE Robotics and Automation Letters*, vol. 10, no. 7, pp. 6975–6982, 2025.
- [24] A. Brij Koolwal, F. Barbagli, C. Carlson, and D. Liang, "An ultrasound-based localization algorithm for catheter ablation guidance in the left atrium," *International Journal of Robotics Research*, vol. 29, no. 6, 2010.
- [25] J. A. Borgstadt, M. R. Zinn, and N. J. Ferrier, "Multi-modal localization algorithm for catheter interventions," in *2015 IEEE International Conference on Robotics and Automation (ICRA)*, 2015, pp. 5350–5357.
- [26] A. Ataka, P. Qi, A. Shiva, A. Shafti, H. Wurdemann, H. Liu, and K. Althoefer, "Real-time pose estimation and obstacle avoidance for multi-segment continuum manipulator in dynamic environments," in *2016 IEEE/RSJ International Conference on Intelligent Robots and Systems (IROS)*, 2016, pp. 2827–2832.
- [27] Y. Chen, S. Zhang, L. Zeng, X. Zhu, and K. Xu, "Model-based estimation of the gravity-loaded shape and scene depth for a slim 3-actuator continuum robot with monocular visual feedback," in *2019 International Conference on Robotics and Automation (ICRA)*, 2019, pp. 4416–4421.
- [28] J. Y. Loo, K. C. Kong, C. P. Tan, and S. G. Nurzaman, "Non-linear system identification and state estimation in a pneumatic based soft continuum robot," in *2019 IEEE Conference on Control Technology and Applications (CCTA)*, 2019, pp. 39–46.
- [29] D. Kim, M. Park, and Y.-L. Park, "Probabilistic modeling and bayesian filtering for improved state estimation for soft robots," *IEEE Transactions on Robotics*, vol. 37, no. 5, pp. 1728–1741, 2021.
- [30] M. Mehl, M. Bartholdt, S. F. Ehlers, T. Seel, and M. Schappeler, "Adaptive state estimation with constant-curvature dynamics using force-torque sensors with application to a soft pneumatic actuator," in *IEEE International Conference on Robotics and Automation*, 2024, pp. 14939–14945.
- [31] R. Peng, Y. Wang, and P. Lu, "A tendon-driven continuum manipulator with robust shape estimation by multiple imus," *IEEE Robotics and Automation Letters*, vol. 9, no. 4, pp. 3084–3091, 2024.
- [32] E. J. Lobaton, J. Fu, L. G. Torres, and R. Alterovitz, "Continuous shape estimation of continuum robots using x-ray images," in *2013 IEEE International Conference on Robotics and Automation*, 2013, pp. 725–732.
- [33] G. Zhang and L. Wang, "Stochastic adaptive estimation in polynomial curvature shape state space for continuum robots," 2025, *arXiv:2210.08427*.
- [34] A. W. Mahoney, T. L. Bruns, P. J. Swaney, and R. J. Webster, "On the inseparable nature of sensor selection, sensor placement, and state estimation for continuum robots or "where to put your sensors and how to use them"," in *2016 IEEE International Conference on Robotics and Automation (ICRA)*, 2016, pp. 4472–4478.
- [35] P. L. Anderson, A. W. Mahoney, and R. J. Webster, "Continuum Reconfigurable Parallel Robots for Surgery: Shape Sensing and State Estimation With Uncertainty," *IEEE Robotics and Automation Letters*, vol. 2, no. 3, pp. 1617–1624, 2017.
- [36] S. Lilge, T. D. Barfoot, and J. Burgner-Kahrs, "Continuum robot state estimation using gaussian process regression on $SE(3)$," *The International Journal of Robotics Research*, vol. 41, no. 13–14, pp. 1099–1120, 2022.
- [37] S. Anderson and T. D. Barfoot, "Full steam ahead: Exactly sparse gaussian process regression for batch continuous-time trajectory estimation on $se(3)$," in *2015 IEEE/RSJ International Conference on Intelligent Robots and Systems (IROS)*, 2015, pp. 157–164.
- [38] S. Lilge, T. Barfoot, and J. Burgner-Kahrs, "State estimation for continuum multirobot systems on $se(3)$," *IEEE Transactions on Robotics*, vol. 41, pp. 905–925, 2025.
- [39] S. Lilge and T. D. Barfoot, "Incorporating control inputs in continuous-time gaussian process state estimation for robotics," *Robotica*, vol. 43, no. 3, p. 1067–1086, 2025.
- [40] J. M. Ferguson, D. C. Rucker, and R. J. Webster, "Unified shape and external load state estimation for continuum robots," *IEEE Transactions on Robotics*, vol. 40, pp. 1813–1827, 2024.
- [41] A. W. Mahoney, P. L. Anderson, P. J. Swaney, F. Maldonado, and R. J. Webster, "Reconfigurable parallel continuum robots for incisionless surgery," in *IEEE International Conference on Intelligent Robots and Systems*, 2016, pp. 4330–4336.
- [42] S. Teetaert, S. Lilge, J. Burgner-Kahrs, and T. D. Barfoot, "Space-time continuum: Continuous shape and time state estimation for flexible robots," 2024, *arXiv:2409.12302*.
- [43] T. D. Barfoot, *State Estimation for Robotics*. Cambridge University Press, 2017.
- [44] D. C. Rucker and R. J. Webster III, "Statics and dynamics of continuum robots with general tendon routing and external loading," *IEEE Transactions on Robotics*, vol. 27, no. 6, pp. 1033–1044, 2011.
- [45] J. Till, V. Aloï, and C. Rucker, "Real-time dynamics of soft and continuum robots based on Cosserat rod models," *International Journal of Robotics Research*, vol. 38, no. 6, pp. 723–746, 2019.
- [46] T. D. Barfoot and P. T. Furgale, "Associating Uncertainty with Three-Dimensional Poses for use in Estimation Problems," *IEEE Transactions on Robotics*, vol. 30, no. 3, pp. 679–693, 2014.
- [47] T. D. Barfoot, J. R. Forbes, and D. J. Yoon, "Exactly sparse gaussian variational inference with application to derivative-free batch nonlinear state estimation," *The International Journal of Robotics Research*, vol. 39, no. 13, pp. 1473–1502, 2020.
- [48] P. T. Dewi, P. Rao, and J. Burgner-Kahrs, "A lightweight modular segment design for tendon-driven continuum robots with pre-programmable stiffness," in *IEEE 7th International Conference on Soft Robotics*, 2024, pp. 531–536.
- [49] M. Shah, "Solving the robot-world/hand-eye calibration problem using the kronecker product," *Journal of Mechanisms and Robotics*, vol. 5, no. 3, p. 031007, 06 2013.